AD-A107 559 CONNECTICUT UNIV STORRS INST OF MATERIALS SCIENCE F/G 20/5
ELECTRON BEAM/LASER GLAZING OF IRON-BASE MATERIALS.(U)
JUL 81 P R STRUTT, B G LEWIS, M KURUP N00014-78-C-0580
UNCLASSIFIED NL

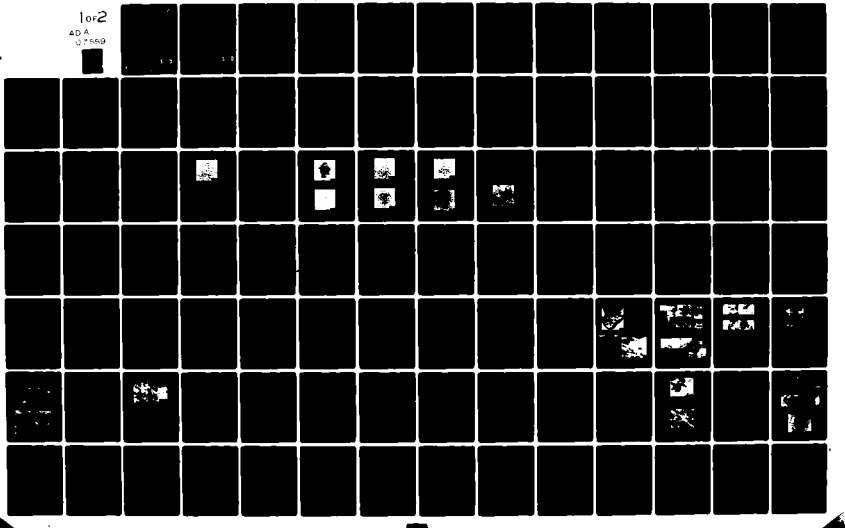

ELECTRON BEAM/LASER GLAZING OF IRON-BASE MATERIALS

P. R. Strutt, B. G. Lewis, and M. Kurup

July 1981

Annual Progress Report

Office of Naval Research
Arlington, Virginia 22217

Contract #N00014-78-C-0580

406676
406916
Metallurgy Department
Institute of Materials Science
University of Connecticut
Storrs, Connecticut 06268

Electron Beam/Laser Glazing of Iron-Base Materials

P. R. Strutt, B. G. Lewis, and M. Kurup

July 1981

Annual Progress Report

Office of Naval Research
Arlington, Virginia 22217

Contract #N00014-78-C-0580

Metallurgy Department
Institute of Materials Science
University of Connecticut
Storrs, Connecticut 06268

SECURITY CLASSIFICATION OF THIS PAGE (When Data Entered)

REPORT DOCUMENTATION PAGE	READ INSTRUCTIONS BEFORE COMPLETING FORM
1. REPORT NUMBER	2. GOVT ACCESSION NO. AD-A107519
	3. RECIPIENT'S CATALOG NUMBER Annual Progress Report July 1981
4. TITLE (and Subtitle) Electron Beam/Laser Glazing of Iron-Base Materials	5. TYPE OF REPORT & PERIOD COVERED
	6. PERFORMING ORG. REPORT NUMBER
7. AUTHOR(s) Peter R. Strutt, B. G. Lewis and M. Kurup	8. CONTRACT OR GRANT NUMBER(s) N00014-78-C-0580
9. PERFORMING ORGANIZATION NAME AND ADDRESS Metallurgy Department University of Connecticut Storrs, CT 06268	10. PROGRAM ELEMENT, PROJECT, TASK AREA & WORK UNIT NUMBERS
11. CONTROLLING OFFICE NAME AND ADDRESS Office of Naval Research Arlington, Virginia 22217	12. REPORT DATE July 1981
	13. NUMBER OF PAGES
14. MONITORING AGENCY NAME & ADDRESS(if different from Controlling Office)	15. SECURITY CLASS. (of this report) Unclassified
	15a. DECLASSIFICATION/DOWNGRADING SCHEDULE

16. DISTRIBUTION STATEMENT (of this Report)

Unlimited

DISTRIBUTION STATEMENT A
Approved for public release;
Distribution Unlimited

17. DISTRIBUTION STATEMENT (of the abstract entered in Block 20, if different from Report)

18. SUPPLEMENTARY NOTES

19. KEY WORDS (Continue on reverse side if necessary and identify by block number)

20. ABSTRACT (Continue on reverse side if necessary and identify by block number)

Research on directed energy source processing of hard-iron base materials demonstrates the effect of environment, alloy chemistry and processing parameters on the nature of the crystal structure, distribution, and compositional variation of phases. In molybdenum high speed steels, for example, it is found that segregation resulting from convective and turbulent flow during glazing may either result in large scale phase separation or compositional variation within a phase. Another example of the importance of processing conditions is

DD FORM 1 JAN 73 1473 EDITION OF 1 NOV 65 IS OBSOLETE

SECURITY CLASSIFICATION OF THIS PAGE (When Data Entered)

a clear demonstration of the effect of small oxide particles in inducing martensite during laser processing.

A detailed analysis has been made to determine the effect of deflection coil parameters on the distortion of surface area glazing patterns. This is particularly important in developing techniques for preparing uniform rapidly solidified layers.

In studying molybdenum base high speed steels the value of the carbon content is found to be important in determining delta ferrite formation and the peritectic reaction of this phase to form austensite and carbide phases. In contrast to M2 (where the carbon concentration is 0.85wt%) a homogeneous γ/α' phase mixture forms in materials with a carbon content of $\geq$1wt%, i.e. the alloys M7, and M42. However in these two materials combined convective and turublent flow during glazing results in a significant composition variation of the refractory elements. Tempering largely removes this inhomogeneity and results in the formation of a homogeneous tempered martensite structure. A most important effect observed in M2, M7, and M42 was the shift to longer tempering times of material glazed at moderate to high beam velocities.

In another part of the study the wear behavior of the steel-base cemented carbide material "Ferro-TiC" SK was studied following electron beam glazing and tempering treatments. The effect of glazing was a three to five fold increase in the wear life in tests using a fully hardened M42 high speed steel counterface.

$> \sigma v =$

INDEX

INTRODUCTION

An intriguing aspect of research conducted within the period of this report is the demonstrated effect of environment, alloy chemistry, and processing parameters on the crystal structure, distribution, and compositional variation of phases in (i) high carbon and (ii) molybdenum high speed steels. As an example, it has been found that segregation resulting from convective and turbulent flow during glazing may either result in large-scale phase separation, or alternatively, compositional variation within a phase. Another example showing the importance of processing conditions during directed energy beam glazing is the striking effect that small oxide particles, formed by absorbed oxygen, have in inducing martensite in a high carbon-low alloy steel. These features, together with a comprehensive description of work on O.N.R. Contract N00014-79-C0580 for the period 30 June 1980 to 30 June 1981 is covered in Sections 1 to 4 in this report.

A detailed analysis is given in section 1 on the effect that deflection coil parameters have in determining the uniformity of surface area glazing patterns. This is particularly important in developing techniques for preparing specimens with high quality surfaces for wear studies and other investigations. Section 2 describes work on high carbon (1 to 1.5wt%), low alloy ($\sim$1.5wt%Cr) steels after laser and electron beam glazing. In this work it is shown that the dramatic difference in microstructure and hardness following processing with the two energy sources is, as already stated, due to oxygen absorption during laser processing.

A major feature of the program, discussed in section 3, is the effect of alloy chemistry on the properties of molybdenum high speed steels. The three materials selected for study were M2, M7, and M42 and the effect of increasing the carbon content from 0.85 to 1.10wt% is to supress delta ferrite formation and the peritectic reaction. As a result of this a more homogeneous γ/α' phase

mixture occurs throughout the melt region in M7 and M42. However in these alloys, particularly in M42, there is a significant compositional variation of the refractory elements which arises from convective and turbulent liquid flow during the glazing process. This section of the report describes the microstructural changes which occur during tempering and the shift of the secondary hardening peak to a longer tempering time.

Fianlly, section 4 describes work on the wear of the steel-base cemented carbide material "Ferro-Tic" SK before and after electron beam surface area glazing. In wear against M42 high speed steel the wear life is found to increase by a faction of between 3 and 5.

SECTION 1

NON-LINEARITIES IN ELECTRON-BEAM SCANNING

NON-LINEARITIES IN ELECTRON-BEAM SCANNING

1. Introduction

Recently, it has been shown that reasonably smooth surfaces are formed by scanning electron-beam glazing (1) using appropriate processing parameters. Depending upon the actual values of the parameters selected, the thickness of a rapidly solidified layer is from 50 to 200 microns. In these studies a scanning mode was used in which the electron-beam traced out a series of rectangular 'Lissajous'figures. The method for producing such a pattern is by applying two nearly equal frequency signals to the X and Y axis deflection coils. This scanning mode was initially applied for acheiving solid state transformation hardening in a steel (2) without actual melting of the material.

Another surface melting mode is that in which the electron-beam is rapidly oscillated by a single set of deflection coils so as to act as a line heat source (3,4). The line heat source is then swept across the surface either by mechanical translation of the workpiece relative to the beam deflection with a second perpendicular set of electromagnetic windings in the deflection yoke.

In all electromagnetic deflection modes the rapidity and linearity of actual beam motion is an important, and often a critical factor. Even with a well-designed deflection yoke assembly, the induction limits the response of the beam to any change in excitation voltage. The effect of this is manifest as non-linearity in beam velocity and noticeable dwell times during reversal of beam direction. With the preceeding consideration in mind we examine in the following sections, the effect of coil and circuit parameters on beam displacement and velocity; also to be discussed is non-linearity in beam deflection patterns.

In considering any beam deflection situation we note that the deflection angle θ of an electron beam as it passes through an electromagnetic yoke is given by equation 1.

$$\sin \theta = \frac{l\mu_o H\sqrt{e/m}}{\sqrt{2E}} \qquad (1)$$

where l is the length of the coil, μ_o the permeability and H_o the intensity of the magnetic field. The accelerating voltage applied between the gun and anode is E and e/m is the usual charge/mass ratio of an electron. The energy stored by the excited coil is 1/2 Li^2, where L is the inductance and i the current. This can also, as given by equation 2, be expressed in terms of the magnetic field energy; equation 2 is, in fact, an energy balance (5).

$$\frac{Li^2}{2} = \frac{\mu_o}{2} \int H^2 dV \qquad (2)$$

If we assume H is constant then

$$\int H^2 dV = H^2(\pi r^2 l) \qquad (2a)$$

where r is the radius and $(\pi r^2 l)$ the volume within the inner coil.

By rearranging equation 2 and combining with equations 1 and 2a we obtain equation 3

$$\sin \theta = \frac{(i/r)\sqrt{Ll\mu_o(e/m)}}{\sqrt{2\pi E}} \qquad (3)$$

The sensitivity obviously $\frac{d\theta}{di}$ increases with increasing $\sqrt{L}$, the detrimental effect of this, however, is a distortion in waveform and a corresponding reduction in frequency response. In our present analysis we will ignore any magnetic hysteresis effects.

2. Current Waveform Analysis

During the application of a triangular waveform voltage to a L-R circuit the appropriate equations during the first and second half of a cycle are given by equations 4a and b

$$\frac{di}{dt} + i(R/L) = (k/L)t; \qquad (4a)$$

$$\frac{di}{dt} + i(R/L) = \frac{K}{L}\left(\frac{\tau}{2} - t\right); \qquad (4b)$$

Where k is equal to 2fV, f being the frequency and V the maximum amplitude of the triangular waveform voltage; (where $\tau = 1/f$) is the half cycle period.

To avoid Fourier analysis a simple reiteration approach gives the pertinent results for the case of exciting a beam deflection coil. Defining a dimensionless current parameter (i/i*) it may be shown that the overall swing of (i/i*) is given by equation 5.

$$(i/i^*) = 1 - \frac{1}{\lambda} \ln (1 + \tanh \lambda) \qquad (5)$$

The value of i* is equal to V/R and λ is the non-dimensional parameter R/4Lf.

Representation of the actual current waveform is most conveniently described in terms of non-dimensional time n, which is equal to 2ft. where t is the time in seconds. During the first half cycle of the applied triangular waveform voltage the corresponding current waveform is given by equation 6a.

$$(i/i^*) = \text{func}(n) = (n - \frac{1}{2\lambda}) + \frac{(1 + \tanh \lambda)}{2\lambda} e^{-2\lambda n} \qquad (6a)$$

The parameter n will vary from 0 to 1 during the first half cycle of the applied voltage signal.

The corresponding equation for the current as the applied voltage decreases during the second half of its cycle is given by equation 6b.

$$(i/i^*) = 1 - \text{func}(n) \qquad (6b)$$

In this case n varies from 0 to 1 as the applied voltage decreases from the maximum value to zero. The profile of the applied voltage signal and the corresponding current signal are shown diagramically in Fig. 1; the phase shift between the two is given by equation 7.

$$\Delta n^* = 1 - \frac{1}{\lambda} \tanh \lambda; \qquad (7)$$

One of the most important aspects of electromagnetically deflecting the beam is the amplitude frequency dependence. A relationship; this may readily be obtained from the analysis and is given by equation 8, which in actuality is a relationship between $(i/i^*)_{amp}$ and λ.

$$(i/i^*)_{amp} = 1 - \frac{1}{\lambda} \ln (1 + \tanh \lambda) \qquad (8)$$

Fig. 2 is a plot from equation 8 of normalized maximum current swing vs. normalized frequency $(1/\lambda)$. This curve is for the case where there is no feed-back control, the effect of feed-back is the reduction of the "roll-off," which occurs with increasing frequency.

3. Scanning Line Heat Source

An important effect, particularly when a rapidly oscillating beam acts as a line heat source, is the prolonged dwell-time when the beam changes direction. To study this behavior it is instructive to plot $(i/i^*)_{amp}$ vs $d(i/i^*)/dt$ since, in effect, this represents a plot of normalized beam velocity vs. normalized beam displacement. If there were no inductance in the circuit the normalized beam velocity would be +1 or -1, the sign depending upon the direction of motion. In actuality, there is a definite region over which the beam velocity progressively increases as the beam moves away from the point of maximum displacement, see Figure 4. Here we see that for $\lambda = 5$ the beam does not attain the limiting velocity until it has moved $\sim$25% the way across the oscillated width. Similar behavior will also occur as the beam moves back from the maximum right hand side displacement. This "dwelling" of the beam towards either end of the oscillated width is clearly considerable. This is particularly so when actual beam penetration occurs since definite groves will be formed in the surface of the material. From Fig. 3, we see that having a significantly high value of λ (equal to R/fLf) is important if one wishes to avoid having

a significant "dwelling" either end of the oscillated width.

4. Distortion of Pattern

As previously discussed (1) a convenient way of obtaining an electron-beam glazed surface is to use a rectangular "Lissajous" figure type of scanning pattern. This is generated by applying two nearly equal frequency triangular waveform signals to the X and Y axis coils of the electromagnetic deflection yoke. The frequency f determines the actual beam velocity and the difference of the time for tracing out one complete frame. In practice the limited response of the deflection coil L-R circuits results in non-linearity in the scanning pattern, although this is minimal at low frequencies. The effect of this non-linearity is readily appreciated by noting the loop shape in Fig. 4, where there is particularly pronounced curvature at the loop corners. It is important to note that there is significant dwelling of the beam within these regions, and as a result a corresponding increase in the depth of melting. In the same cases the dwelling may be sufficient for actual penetration of the beam into the material which results in the formation of definite grooves.

The electron-beam path in Fig. 4 was deduced theoretically using equations 6a and b in the previous analysis assuming a value of 5.5556 for the parameter λ (which is equal to R/4Lf). The frequencies assumed 100 and 105 hertz, corresponding to a value of $\Delta f/f$ of 0.05. It is pertinent to note that the value of λ assumed is obtained using the coil parameters of a typical commercial electron-beam welder deflection yoke, namely an inductance of 45 millihenries and a resistance of 100 ohms.

To obtain improved "Lissajous" patterns with negligible distortion calculations show that λ should be equal to or greater than 50. Further improvement in response at higher frequencies is acheivable using feed-back circuiting with high "slew-rates" ranging from 10 to 1000 volts per millisecond are obtainable.

References

1. P. R. Strutt, Materials Science and Engineering, 49 (1981) 87-91.

2. R. Mayer, W. Dietrich and D. Sundermeyer, Weld. J. (Miami), 56 (1977) 35.

3. W. Gruhl, B. Grzemba, G. Ibe and W. HIller, Aluminum, 53 (1977) 177.

4. T. R. Tucker, J. D. Ayers and R. J. Schaefer, Laser and Electron Beam Processing of Materials, Academic Press, New York, 1980. p. 760.

5. H. C. Masterman, Electronics Design, February, 1979.

FIGURE CAPTIONS

Fig. 1 Relative forms of the (i) input voltage and (ii) coil current waveforms. The change in waveform and phase of the current signal is a function of the value of the R/4Lf parameter.

Fig. 2 Normalized current amplitude as a function of normalized frequency; this may be used, for example, to determine the decrease in current amplitude with increasing frequency.

Fig. 3 Normalized beam deflection rate as a function of coil current; the improved linear response with using a higher value of λ is clearly evident.

Fig 4 Distorted rectangular Lissajous' figure pattern obtained from a beam deflection system with a small value of the R/4Lf parameter.

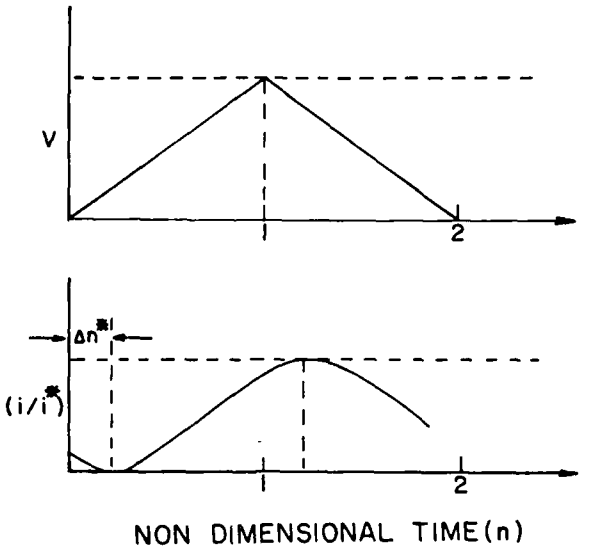
V
2
Δn*
(i/i*)
2
NON DIMENSIONAL TIME(n)

Fig.1

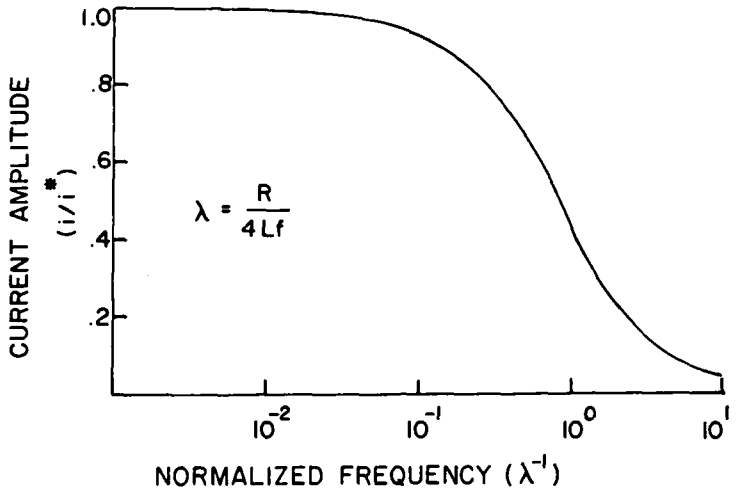
1.0
.8
.6
.4
.2
CURRENT AMPLITUDE
(i/i*)
λ = R/4Lf
10^-2
10^-1
10^0
10^1
NORMALIZED FREQUENCY (λ^-1)

Fig.2

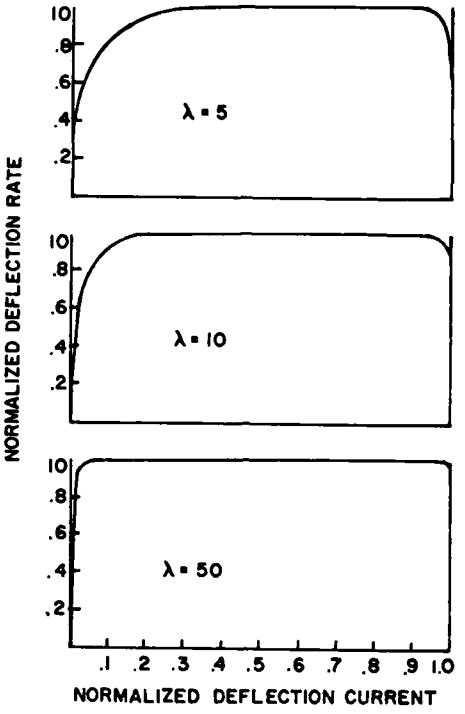
NORMALIZED DEFLECTION RATE
λ = 5
λ = 10
λ = 50
.1 .2 .3 .4 .5 .6 .7 .8 .9 1.0
NORMALIZED DEFLECTION CURRENT

Fig.3

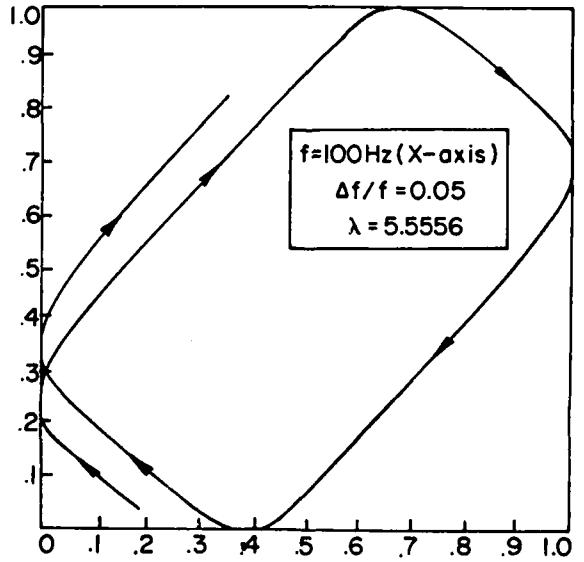
f=100Hz (X-axis)
Δf/f = 0.05
λ = 5.5556
0 .1 .2 .3 .4 .5 .6 .7 .8 .9 1.0

Fig.4

SECTION 2

LASER AND ELECTRON-BEAM GLAZED HIGH CARBON STEELS

LASER AND ELECTRON-BEAM GLAZED HIGH CARBON STEELS

Introduction

Recently, it has been shown that sub-micron grain size high carbon steels (1.3 to 1.5 wt% carbon) have attractive properties following thermomechanical heat treatment (1). In particular, a high hardness approaching 300 V.H.N. is accompanied by good compression ductility, which is of the order of ∿10%. The predicted M_s temperature for these materials using a well known empirical relationship (2) ranges from -61°C for the 1.3 wt % C alloy to -121°C for the 1.5wt% C alloy. In the heat treatment of these materials, however, the formation of carbides obviously raises the M_s temperature.

In view of the desirable properties of highly refined thermomechanically processed material it is of interest to determine if comparable results may be obtained using other methods. For this reason experiments were undertaken using laser surface melting and laser electron beam surface melting. In considering the work to be presented it is worth noting that Sunada, Wadsworth, Lin and Sherby (1) controlled the hardened state by first selecting the austenitizing temperature. The austenite grain size was varied by heat treating at various temperatures between 1150°C to 750°C; the minimum grain size was ∿0.6μm. In the fully hardened condition the maximum hardness was 900 V.H.N. This was shown to result from a martensitic structure on a scale as to be only resolvable using transmission electron microscopy. Interestingly, this morphology corresponds to the optically unresolvable phase observed in high carbon steels many years ago by Sauveur (3).

For reference in the following discussion of the laser and electron beam glazing experiments, the microstructure in thermomechanically processed 52150 steel following two stage austenitizing is shown in the scanning electron micrograph in Fig. 1. This material in the as thermomechanically processed condition was kindly supplied by Professor Sherby with an analysis as given in Table I.

The complete austenitizing and quenching history is as shown in Fig. 2; holding time at 850°C and 750°C are of 30 minutes. The grain size in Fig. 1 is about 1 to 2 μm and in such a microstructure previous thin-foil observations by Sunada et al. (1) reveal a martensitic structure which is predominantly twinned in character. In addition, there is a relatively uniform distribution of cementite particle which are a residue of the original thermomechanically processed microstructure. Their existence naturally reduces the carbon concentration within the matrix and hence increases the M_s temperature.

Laser Glazing Experiments

The laser glazing experiments were carried out using a continuous CO_2 laser with a beam diameter of 0.5 mm and beam power of 5.1 kW. Values of microhardness at various beam velocities are given in Table II together with values obtained after quenching post-glazed specimens into liquid nitrogen. Apart from the soft condition obtained by glazing at the lowest beam velocity ($5cm.s^{-1}$) there is a pronounced hardening following processing which progressively increases with increasing beam velocity, see Fig. 3. Subsequent liquid nitrogen quench only produces further hardening in the specimen glazed at 5 $cm.s^{-1}$ which is in a soft condition, see Table II.

At low magnification (X1600) the scanning electron micrograph of the cross-sectional view of the melt zone in Fig. 4 exhibits a discernable directionality arising from the solidification dendritic structure. This particular micrograph is of a melt zone formed at a beam velocity of 25 $cm.s^{-1}$; the corresponding microhardness is 745 V.H.N., see Table II. In contrast to Fig. 1 there is no evidence of a carbide particle distribution. Since electron beam glazing produces a particularly clean surface the directionality of the solidification structure is readily appreciated by viewing the as-melted surface, a scanning electron micrograph of such a view is seen in Fig. 5. Returning to laser melted structures, the enlarged portion of Fig. 3 shown in Fig. 6 reveals that the grains tend to be irregularly shaped in contrast to the equiaxed grains in the two-step austenitized and quenched material (Fig. 1).

In comparing microstructures in the normal and laser treated specimens, see Figs. 1 and 6, it is important to note the striking difference in the processing times involved. As seen from Fig. 2, the total heat treatment processing time exceeds an hour, whereas that for laser treatment is only a few milliseconds. Furthermore, optimum hardness is attainable without subsequent quenching into liquid nitrogen. It is interesting to find that the effect of increasing the beam velocity and hence decreasing the processing time is to further increase the microhardness, see Table II. The finer scale, but similar type, microstructure formed at a higher beam velocity (75 $cm.s^{-1}$) is seen by the micrograph in Fig. 7.

Electron Beam Glazing

The electron beam glazing was carried out in a modified Carl Zeiss electron beam unit at the Metallurgy Department, University of Connecticut. The vacuum during actual glazing was $\sim 10^{-5}$ Torr; this is in contrast to the laser-glazing experiments in which specimens are processed in a hood with a flowing helium atmosphere. Owing to the difference in coupling efficiency (3) of the laser and electron beam with a material the beam power for electron glazing was 375 watts; this compares with 5.1 kW beam power for the laser glazing experiments. At these power levels a similar melt depth was obtained for a given beam velocity with both irradiation sources. In one particular case a wide beam (1 mm) produced by rapid beam oscillation was used instead of a circular spot; the beam velocity relative to the melting direction was 3.5 $cm.s^{-1}$.

Very surprisingly, the microhardness following electron beam glazing was relatively low, ranging from 350 to 450 V.H.N., see Table II. Furthermore, microscopy did not reveal any evidence of any martensite structure. In fact, in the scanning electron micrograph in Fig. 8, the structure is relatively featureless apart from the voids formed in interdendritic regions due to the heavy etching. In the vicinity of these voids there appear to be small cementite particles tending, in some instances, to be thin and elongated. Another surprising finding was that

the response of the as-glazed material to liquid nitrogen quenching was particularly erratic, see Table II. In each case there is seen to be at least a detectable increase in hardness, and in some instances a significant increase, following quenching into liquid nitrogen. The highest attainable hardness value (1050 to 1100 V.H.N.) was produced by quenching the specimen with the particularly wide melt zone (1 mm) into liquid nitrogen. As previously stated this zone was obtained by rapidly oscillating the beam with one set of deflection coils. The microstructure corresponding to this particularly impressive hardened state for a 52150 steel is shown in Fig. 9. Here the plate martensite structure is well defined and on a coarser scale to that observed by Sunada et al. (1) following normal heat treatment in foil specimens.

In studying electron beam glazing of high carbon-low alloy steels, it is pertinent to note a hardened martensitic structure is formed following actual glazing when the carbon content is reduced to 1 wt %. This is to be expected since the normal M_s temperature for this material is $\sim$60°C.

Carbon Content Analysis

In finding the underlying reason why the M_s temperature is apparently increased by laser glazing it is important to check if processing produces a significant change in carbon content. A loss would naturally increase the M_s temperature which possibly might be sufficient for martensite formation well above room temperature.

Precise carbon content measurements were made within the melt zone and the parent material using wavelength dispersive analysis. The system employed was the microspec WDX-2A attachment to the AMRAY 1000/1000A. A procedure was adapted to remove possible error due to possible compositional change due to chemically etching the sample. This involves making small diamond indentations for the subsequent location of melt zones in the polished and etched sample. For viewing in the scanning electron microscope the etched layer is removed by light mechanical polishing. Previous chemical analysis had shown that the carbon concentration in

the 52150 steel was 1.48wt%. This value was then used for calibration purposes in determining the values within the melt zones. Actual peaks obtained from the wavelength spectrometer are seen in Fig. 10. The three peaks correspond to regions within the (a) parent material, (b) melt zone formed with a beam velocity of 25 $cm.s^{-1}$, and (c) melt zone formed with a beam velocity of 110 $cm.s^{-1}$. The curves are identical in shape and comparable in scale, calculated values of the carbon concentration as determined from the area beneath such curves are given in Table III. From this table there is seen to be no carbon loss in the single pass shallow melt zone ($\sim$60 μm deep) formed by glazing at a high beam velocity (110 $cm.s^{-1}$). There is a $\sim$12% reduction in carbon content, however, in a deep melt zone ($\sim$250 μm) following glazing at a low beam velocity (25 $cm.s^{-1}$). An interesting result is the progressive reduction in carbon content in three adjacent overlapping passes, as might, for instance, be formed during surface area scanning.

Glazing Environmental Effect

The totally different type of microstructures obtained following laser and electron beam glazing of 52130 and 52150 steels is rather surprising. Previously it had appeared that the only difference in using these energy sources for glazing was the coupling efficiency between the beam and material (3). The present work indicates that there are additional factors which need to be considered in some instances. The factors could be the type of processing environment and the nature of the fluid flow (i.e. the degree of turbulence and magnetic stirring). In considering the effect of environment, it should be noted that the protective helium atmosphere used in the laser processing, whilst greatly restricting exposure to oxygen, does not entirely eliminate oxide formation. On the basis of models for martensite nucleation (4-6) the small oxide particles formed during the melting process may serve as martensite nucleation sites during cooling in the solid state. Since oxidation is dramatically reduced during melting in the electron beam unit (the vacuum is $\sim 10^{-4}$ to 10^{-5} Torr), martensite nucleation

at oxide particles will be insignificant and hence the microhardness if low. If other types of micro-inclusions and small precipitates are capable of acting as martensite nucleation sites in the case of electron beam melting then electromagnetic stirring may be effective in retarding the formation of a martensitic structure. Certainly, the effects of convective flow, turbulence and electromagnetic stirring (using the electron beam) are important in determining the nature of the microstructures observed in many instances.

Clear evidence showing that absorbed oxygen within the melt during the glazing processing of the 1.5 wt % C steel is afforded by an additional experiment which will now be described. In this electron beam glazing experiment oxygen was introduced by processing a surface with a significantly thick oxide layer. The existence of the small oxide particles within the solidified material was found to induce the formation of a microstructure identical to that previously observed in laser glazed 1.3 wt % C steel. This experiment convincingly shows that the totally unexpected difference originally found between laser and electron beam glazed specimens is environmental in origin.

The microstructure formed in the oxidized electron beam glazed specimen is seen in the scanning electron micrograph in Fig. 11. This figure strikingly resembles Fig. 4 which is for a laser-glazed specimen with a beam velocity of 25 $cm.s^{-1}$. The processing conditions for the electron beam glazed specimen in this particular case are beam power 187.5 watts, beam diameter 0.045 cm, and beam velocity 25 $cm.s^{-1}$. On the basis of these values and assuming a 54% coupling efficiency between beam and substrate the solid state portion of the cooling rate is computed using the model described by Greenwald, E. M. Breinen and B. H. Kear (7). Two cooling curves are given in Fig. 12, one corresponds to the surface and the other to the maximum melt depth; the latter is 75 μm below the surface. This, incidentally, compares with ∿60 μm as measured from a micrograph of the cross-sectional view of the melt zone. In Fig. 12 it is apparent that nearly identical cooling curves are obtained for solid state cooling at the top and bottom of

the melt zone. Thus, as far as solid state transformations are concenred we are justified in assuming uniform cooling throughout the glazed region.

Comparison of Figs. 2 and 12 is particularly intriguing since the totally different types of thermal histories involved give rise to nearly identical microstructures and material properties. In one case the resultant austenitic grain size is produced by relatively prolonged heat treatment of thermally processed material within the temperature range 1150 to 750°C. Whilst in the other a similar scale (or even finer) austenitic grain morphology is produced by rapid solidification. Cooling, in this case, occurs within ∿5 milliseconds in the austenite range and in about 0.1s in the tempering range. In summary, Table IV briefly shows the conditions for producing the fine grain hardened microstructure in the 1.3 and 1.6 wt % C steel materials by (i) thermomechanical processing and heat treatment, (ii) laser glazing, and (iii) electron beam glazing.

References

1. H. Sunada, J. Wadsworth, J. Lin and O. D. Sherby, Mat. Sci. and Engr., 38 (1979), 35.
2. E. R. Petty, Martensite, Longmans Press, London, 1970.
3. P. R. Strutt, Mat. Sci. and Engr., 44 (1980), 239.
4. A. R. Entwisle, Met. Trans., 2 (1971), 2395.
5. J. M. Galligan and T. J. Garosshen, Nature, 274 (1978), 664.
6. M. Suenaga, and H. E. Cook, Acta Met., 28 (1980), 423.
7 L. E. Greenwald, E. M. Breinan and B. H. Kear, pp. 189, in Laser-Solid Interactions and Laser Processing, S.D. Ferris, H. J. Leamy, and J. M. Poate, ed.; Amer. Inst. of Physics, New York, NY, 1979.

Table I

Element	C	Cv	Mn	Si	Mo	V	Ni	Al
weight percent	1.48	1.34	0.56	0.07	0.02	0.01	0.02	0.01

Table II

Electron Beam

Beam Velocity ($cm.s^{-1}$)	0.5	3.5*	5.0	30	60	70	75	80	90	110	125
Hardness (V.H.N.)	430	355	395	405	355	360	345	350	360	390	350
After Liquid N_2 Quench	750	1075	680	425	505	500	505	600	400	800	460

Laser

Beam Velocity ($cm.s^{-1}$)	5.0	25	50	75	100	125
Hardness (V.H.N)	350	745	810	870	875	910
After Liquid N_2 Quench	760	775	820	830	860	920

MICROHARDNESS OF ELECTRON BEAM AND LASER MELTED SPECIMENS
(BEFORE AND AFTER LIQUID NITROGEN QUENCH)

*Melted using 1mm wide oscillated beam

Table III

Treatment	Carbon Content (weight percent)
Parent (as thermomechanically processed)	1.48
110 $cm.s^{-1}$ (overlapping pans)	1.445
25 $cm.s^{-1}$ (single pan)	1.294

Carbon analysis using wavelength dispersive system.

Table IV

Process	Conditions	Hardness (V.H.N.)
Normal heat treatment	850°C 1/2 hr. and 750°C 1/2 hr.	600
Laser glazing	75 $cm.s^{-1}$ beam velocity	850
Electron beam glazing*	25 $cm.s^{-1}$ beam velocity	890

*glazed with oxide surface layer

Summary of Processes producing fine grain size-martensitic strengthened microstructures.

FIGURE CAPTIONS

Fig. 1 Microstructure following austentizating at 850°C for 1 1/2 hrs., and at 750°C for 1 1/2 hrs., followed by quenching into liquid nitrogen.

Fig. 2 Temperature-time diagram showing the thermal history in the double austenitizing and quenching treatment used to obtain the microstructure in Fig. 1.

Fig. 3 Microhardness of as-glazed material following laser and electron beam processing, shown as a function of beam velocity.

Fig. 4 Scanning electron micrograph showing microstructure following laser melting at a beam velocity of 24 $cm.s.^{-1}$, the microhardness is 745 D.P.N.

Fig. 5 Scanning electron micrograph showing the dendritic structure in the as-melted surface following electron beam melting, the beam velocity is 25 $cm.s.^{-1}$.

Fig. 6 Enlarged region of the laser-melted microstructure.

Fig. 7 The higher cooling rate microstructure formed by laser melting at a higher beam velocity (75 $cm.s.^{-1}$).

Fig. 8 The relatively featureless microstructure in electron beam glazed material using a beam velocity of 25 $cm.s.^{-1}$. The voids in interdendritic regions are formed by heavy etching.

Fig. 9 The martensite structure formed following melting a related steel (52100) having a lower carbon content of 1wt%.

Fig. 10 Scanning Auger spectroscopy peaks used to determine the carbon concentration.

Fig. 11 Microstructure formed by electron beam melting 52150 in which a thick oxide layer was formed prior to processing. Note, the similarity of this structure to that obtained by laser surface melting.

Fig. 12 Solid state cooling curves following electron beam melting, curves A and B refer to points situated at the top and bottom of the melt zone, see text for details.

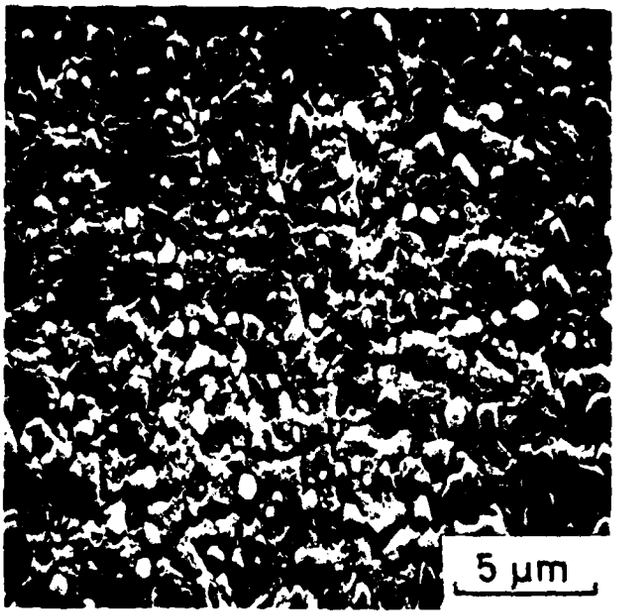
5 µm

Fig. 1

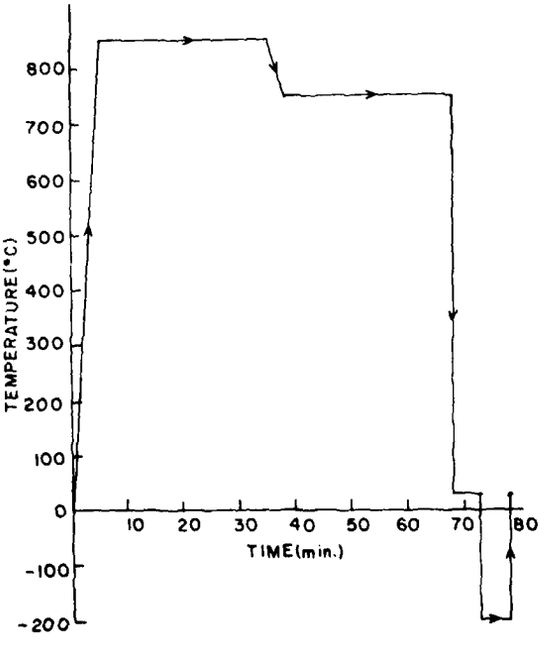
TEMPERATURE(°C)
800
700
600
500
400
300
200
100
0
-100
-200
10
20
30
40
50
60
70
80
TIME(min.)

Fig. 2

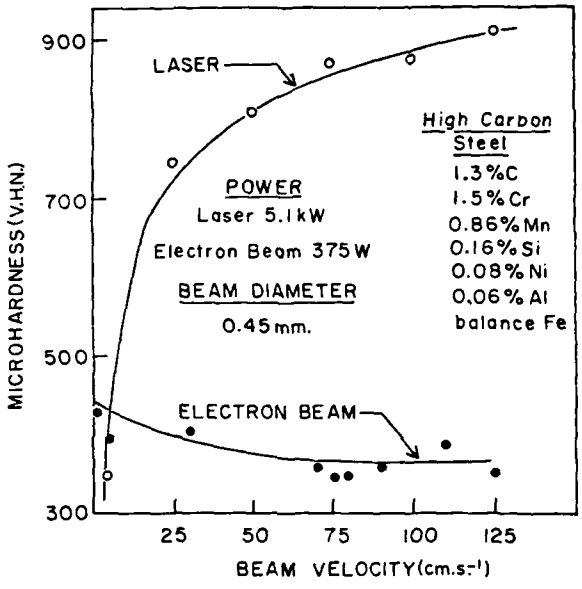
900
700
500
300
MICROHARDNESS (V.H.N.)
LASER
ELECTRON BEAM
POWER
Laser 5.1 kW
Electron Beam 375 W
BEAM DIAMETER
0.45 mm.
High Carbon Steel
1.3% C
1.5% Cr
0.86% Mn
0.16% Si
0.08% Ni
0.06% Al
balance Fe
25
50
75
100
125
BEAM VELOCITY (cm.s⁻¹)

Fig.3

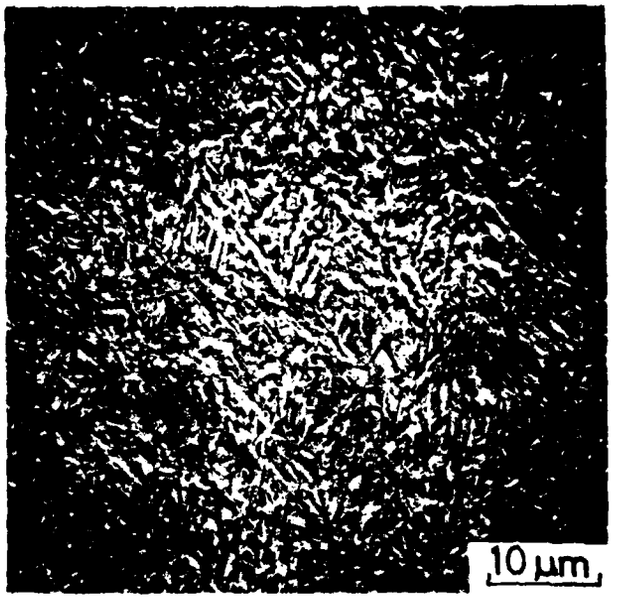

Fig.4

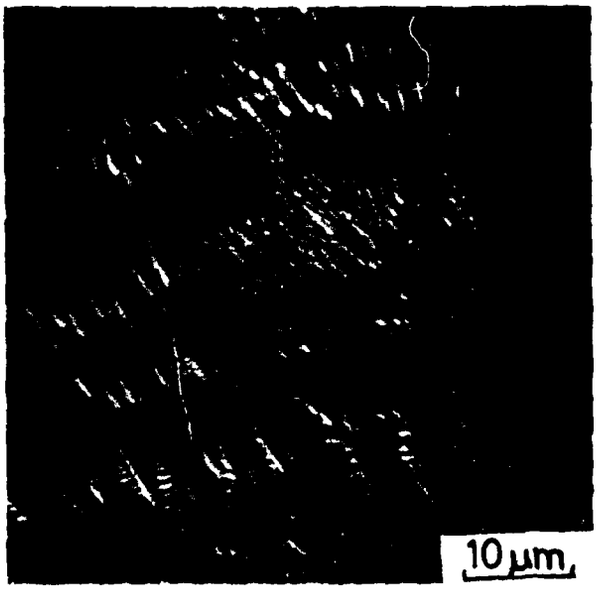

Fig.5

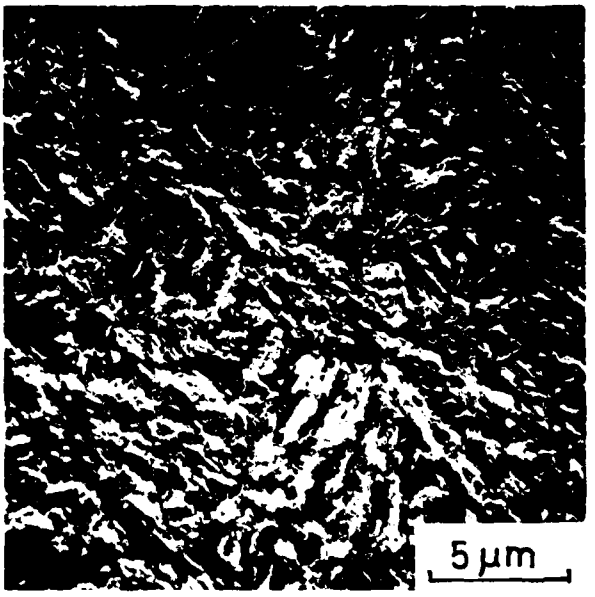

Fig.6

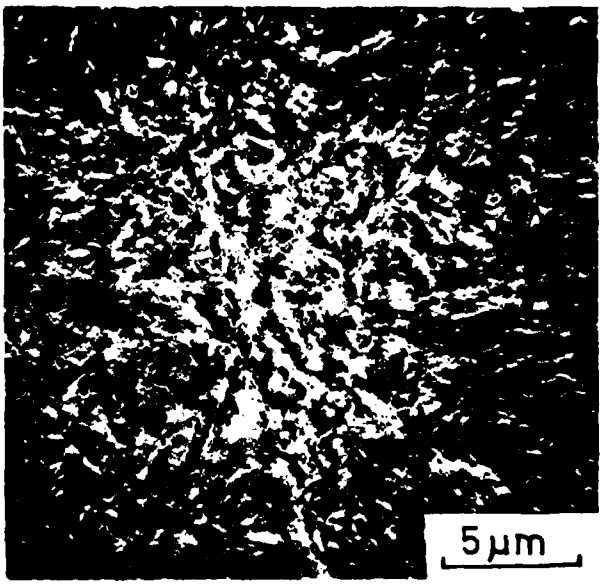

Fig.7

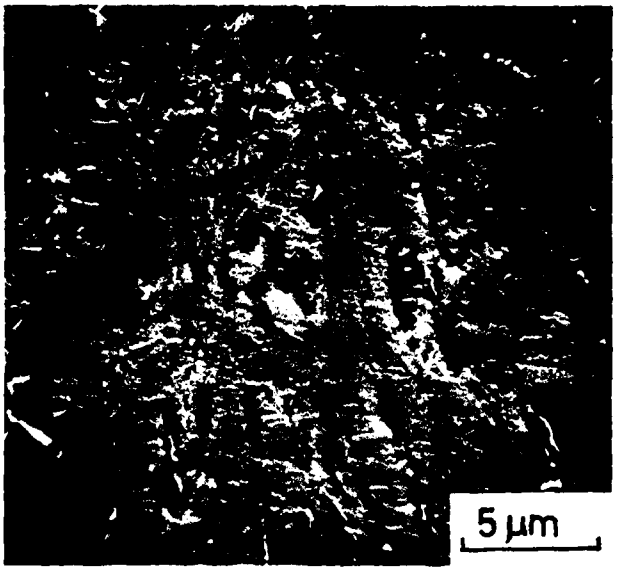

Fig.8

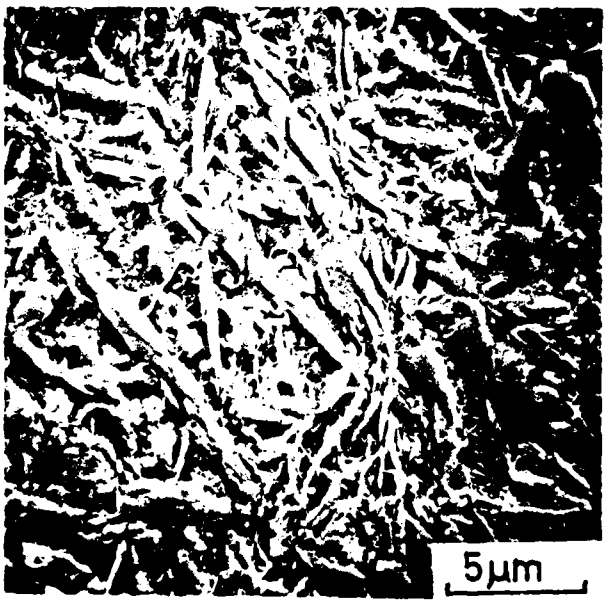

Fig.9

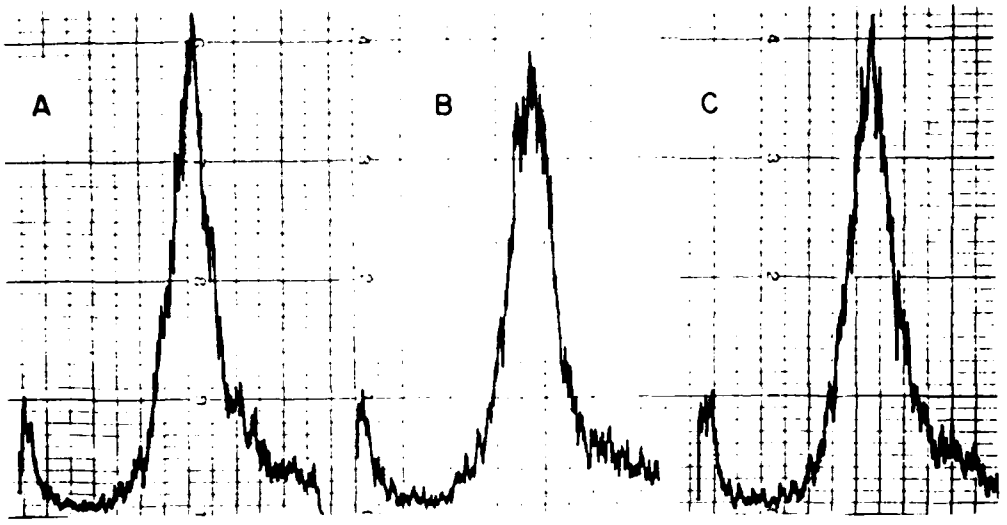

Fig.10

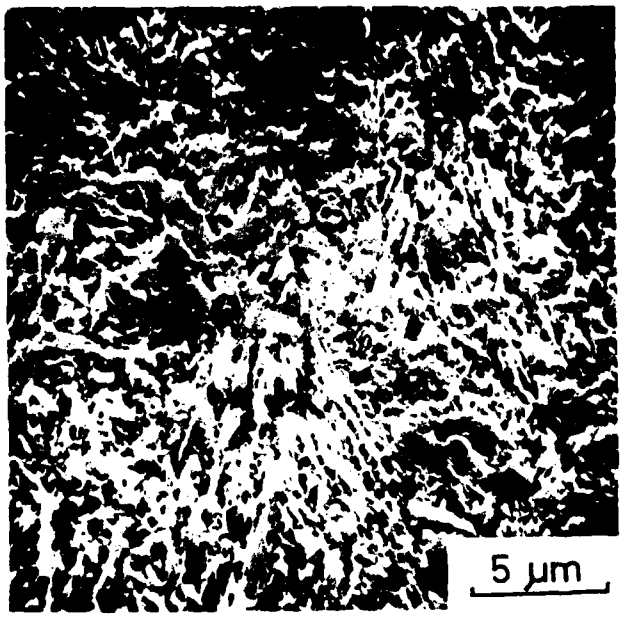

Fig.11

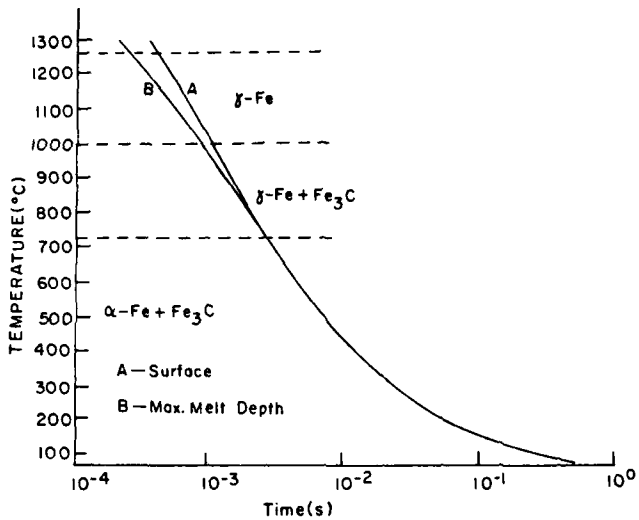
1300
1200
1100
1000
900
800
700
600
500
400
300
200
100
TEMPERATURE(°C)
B
A
γ-Fe
γ-Fe + Fe3C
α-Fe + Fe3C
A—Surface
B—Max. Melt Depth
10-4
10-3
10-2
10-1
100
Time(s)

Fig.12

SECTION 3

ELECTRON BEAM GLAZED TOOL STEELS

M-SERIES-A COMPARATIVE STUDY

ELECTRON BEAM GLAZED TOOL STEELS

M-SERIES, A COMPARATIVE STUDY

1. INTRODUCTION

Recent studies on the effect of laser and electron-beam glazing of molybdenum tool steels, carried out at the Metallurgy Department, University of Connecticut, clearly demonstrate the degree of microstructural refinement and control attainable using these techniques. A salient feature in this work is the importance of subsequent heat treatment in obtaining different (i) crystal structure, (ii) size and (iii) distributor of the carbide precipitate. Another critical factor, not previously investigated is the effect of alloy chemistry both on factors (i) to (iii) and also on the characteristics of the matrix.

In considering any class of alloy, such as the molybdenum tool steels, the precise role of alloy chemistry is complicated since a variety of microstructural characteristics are involved. The matrix hardness which should be as high as possible is, of course, dominated by the hardening response of tool steel - that is the hardness after austenitizing. This comprises solid solution hardening and the strength of the quenched in martensite. A further contribution to the matrix hardness is the secondary carbide precipitation hardness that occurs on tempering.*

The strength of martensite before tempering has been expressed as (1,2)

$$\sigma_y = \sigma_i + \sigma_s + K_y D^{-1/2} + K_y d^{-1/2} + \alpha G b \rho^{1/2}$$

* See Appendix I

where σ_i, K_y and α are constants, G is the shear modulus, b is the Burgers vector of the dislocation, σ_s is from solid solution hardening, ρ is the dislocation density and D, the martensite packet size and d, the martensite lath width are related to grain size. From this equation, the importance of solution hardening and grain size are clear. Improvement in solid solution hardening could be brought about by increasing elemental concentrations beyond solubility limits. Pickering and Gladman (3) have calculated the relative effects of various elements in producing solid solution hardening of ferrite and this work indicates carbon and nitrogen followed by phosphorous and silicon, the interstitials, have the greatest effect with Mo, W, and V having an equal and small effect even though they have a larger solubility in ferrite. (Chromium has a significant negative effect.)

Matrix hardness produced by secondary hardening is more complex again since little work has been done to identify the small precipitated carbides. They include VC, Mo_2C and W_2C. However, tool steels have been developed systematically eliminating W, Mo and V so that none of these elements is essential for precipitation hardening, all that is required is the presence of one of these elements.

Intimately tied in with the above factors is the effect of austenitizing temperature on the as quenched hardness. As the austenitizing temperature is raised, the % retained austenite (γ) present at room temperature is increased (% martensite (α') reduced) and the % carbides undissolved decreases. Coupled with this is an increase in the (prior) austenite grain size with increasing austenitizing temperature (and time). There is thus an optimum austenitizng temperature, below which austenite is formed having such a low carbon content that the martensite developed on quenching has a low hardness, and above which the carbon

and chromium content is high enough to depress the martensite finish (M_f) temperature below about 25°C therefore increasing the retained austenite volume. In the latter case, however, high hardness can be finally achieved following tempering. The secondary hardening peak will be shifted to high temperatures (longer times) but the ultimate hardness will not differ and may even exceed the optimum treatment hardness. However some property loss will arise from the increased grain size.

The importance of modifying the composition of high speed steels for specific applications has been well recognized, and for this reason an entire class of molybdenum-base alloys has been developed from the prototoype M1. For example, in M7 the increased carbide and vandanium additions enhance wear resistance due to the greater amount of hard VC carbides. In another alloy of this class, namely M42, the substantial cobalt addition enhances the hot hardness and is used for the machining of titanium alloys and nickel-base super alloys in the aircraft industry.

In considering the rapidly solidified properties of high speed steels the role of alloy chemistry is clearly an important factor to be investigated. Studies (4) on splat-quenched Fe-X-C alloys show that the phases present in the rapidly solidified specimens are sensitively dependent, in some cases, upon composition. Specifically, in an alloy with a 10 to 15wt% molybdenum addition the dominent phase was either austenite, or martensite depending upon whether the carbon content was less than or greater than ∿1wt%. Thus the unpredictable change in the preponderance of the two phases in laser/electron beam glazed M2 may reflect phase instability for a carbon content of ∿0.85wt%.

A major factor in the study of rapidly solidified high speed steels is the effect of subsequent heat treatment. Such effects have previously studied in laser/electron beam glazed specimens of M2 (5,6).

However, it is particularly intriguing to note, that Rayment and Cantor (7) found that different splat-quench high speed steels responded differently to tempering treatments. A noteworthy finding was the increase in hardness and shift in the tempering peak (by ~100°C) in M42 which had been splat-quenched.

In view of the preceeding considerations a study has been undertaken to elucidate the effect of alloy chemistry on the properties of electron beam glazed molybdenum high speed steels. The alloys used in the comparative investigations are M2, M7, and M42. The latter alloys were selected because of their higher carbon concentration, i.e. 1.0 and 1.1wt% as compared with 0.85wt% in M2. As indicated by splat-quenching studies the increase in carbon content stablizes austenite. The alloy M42 was specifically selected to examine its tempering characteristics which from the work of Rayment and Cantor (7) appear to be of considerable interest.

The object of the work was thus to identify and compare the microconstitutents of rapidly quenched electron beam surface melted tool steels, to compare their tempering response and to assess the possibility of structure/heat treatment modifications by local mircroalloying during melting. Following the results of this investigation, it is intended to screen a series of model alloy systems of a less complex nature including extensive thin foil TEM work to elucidate further the fundamental mechanisms involved in rapid solidification.

2. EXPERIMENTAL TECHNIQUES

Samples of M42 and M7 were cut from bar stock of analyzed composition (Table I) and following conventional austenitizing and quenching were electron beam glazed at four beam velocities (100, 50, 25 and

10 cm.s.$^{-1}$) using a beam power of 300 watts (75 kV, 4mA) at a (measured) beam diameter of 0.3mm. These conditions imposed cooling rates in the range $5x10^6$deg.C.s.$^{-1}$>$\dot{T}$>$5x10^4$deg.C.s.$^{-1}$ respectively.

Table I

Major Alloying Elements* (wt%) in M2, M42 and M7

	C	Cr	W	V	Mo	Co	Mn	Si	Fe
M2	0.84	4.45	6.34	1.95	4.94	0.12	0.30	0.30	Bal
M42	1.09	3.70	1.36	1.12	9.62	7.88	0.24	0.40	Bal
M7	1.01	3.60	1.65	1.82	8.31	----	0.29	0.29	Bal

All other elements <0.01wt%. *Laboratory Test Report

The as-glazed samples were sectioned and specimens were further heat treated by single tempering, double tempering and re-austenitizing and quenching. The actual conditions adopted for each steel are given in Table II. These specimens were then examined using metallographic

Table II

Heat Treatment of M2, M42 and M7

	Austenitizing Temperature	Single Temper	Double Temper†
M2	1205°C (warm oil quench)	1 1/2 hrs, 560°C (air cool)	Further 1 hr, 560°C (air cool)
M42	1190°C (warm oil quench)	2 1/4 hrs, 538°C (air cool)	Further 1 hr, 538°C (air cool)
M7	1195°C (warm oil quench)	2 hours, 538°C (air cool)	Further 1 hr, 538°C (air cool)

†Triple tempering included a further 1 hour at temperature.

techniques that included scanning electron microscopy, electron microprobe analysis (EDAX and WDX), light microscopy and microhardness determinations using a Vickers diamond at 50 gm load.

3. AS-GLAZED SOLIDIFICATION PATTERNS AND RELATED PHASE DISTRIBUTION

3.1 Morphologies in M2; Fluid Flow effects

The microstructure and phases in laser and electron beam glazed M2 high speed steel have been previously discussed by the present authors (5, 6, 8, 9). The overall microstructural character of material following laser-glazing treatment is shown schematically in Fig. 1a. Detailed analysis shows that cellular δ-ferrite exists within the darkly shaded region at the top of the melt zone. It is pertinent to note that in actual micrographs δ-ferrite readily etchs to a dark tone using Vilellas reagent whereas austenite and untempered martensite are lightly etched. In Fig. 1a the larger more lightly shaded region represents a zone in which austenite (γ) and carbide phases form by the ternary peritectic reaction δ + liquid $\rightarrow \gamma$ (+ carbide). This reaction proceeds to a greater extent and eventually to completion as one moves further into the melt zone. The degree of microhardness within this region ($\sim$850 V.H.N.) is typical of that for untempered martensite, however no martensite platelets are observed (9). Finally, in the thin rim near the maximum extent of melting exist a region with a particularly high microhardness which is highly resistant to chemical attack. Although martensite is undiscernable in as-glazed material it is readily revealed by even a short tempering treatment. For example, it is clearly seen in as-glazed scanned surfaces where each individual glazed pass is tempered by heat dissipating from adjacent passes.

In comparable electron-beam glazing experiments on the same alloy there are interesting differences from the behavior just discussed for laser-glazed material. To make the results obtained from the two irradiation source as comparable as is possible the power level of the electron beam was adjusted to give the same depth of melting as the laser; the interaction time using each power source was the same. In contrast to Fig. 1a. the darkly etching region (δ-ferrite) is less extensive as is shown diagrammatically in Fig. 1b., also the amount of δ-ferrite present is extremely variable even for a fixed set of process parameters. Although in some micrographs the phase distribution may appear to be somewhat irregular, see Fig. 2(a) the general tendancy to be like that depicted in Fig. 1b. is well evident. The pattern in Fig. 1b strongly suggests a segregation distribution associated with typical convective flow as shown in Fig. 1d., this type of behavior has previously been considered in other alloy systems (10).

Microscopic observations in the electron beam unit during actual glazing shows turbulent flow in the melt zone, this is particularly so at high glazing velocities and also at just before the melting moves into the deep penetration mode (8). The onset of instability in the idealized streamlined flow, see Fig. 1d, leads to eddy formation. When there is a significant amount of turbulence a microstructure as depicted in Fig. 1c is possible and is frequently observed in electron beam glazed M2 high speed steel Fig. 2(b). Such a microstructure arises in an alloy in which turbulence highly distorts the isothermal surfaces in the melt zone. As a result of this, randomly distributed regions within the melt zone either cool more or less rapidly than in an ideal situation.

The erratic nature of the microstructure thoughout the melt zone in electron beam glazed material would seem to arise from phase instability in rapidly solidified M2 for which clear evidence exists (4). As can be observed for model ternany alloys (4) a 0.85wt% carbon content is close to a critical value and lies within the peritectic (δ)composition such that δ forms at lower values and γ forms at higher values of carbon content. Consequently in M2 (where the amount of C is $\sim$0.85 wt%) segregation and thermal effects due to convective flow and turbulent pertubations can be decisive in determining the relative amounts of the γ and δ phase that form. In view of this it is of considerable interest to examine the situation for alloys with a higher carbon content such as M7 and M42; this is discussed in detail later in this section.

The underlying reasons for the different overall as-glazed solidification pattern in laser and electron-beam irradiation material is strikingly evident, see Fig 1a and b. However another feature of electron beam glazed material is that the characteristic "peritectic reaction" microstructure with cells containing δ-ferrite and transformed γ is not observed. At present the detailed microstructural differences produced by laser and electron beam glazing M2 high speed steel is unclear. But as shown in another section of this report the different microstructures produced by glazing a high carbon-low alloy steel with these two energy sources is due to oxygen absorption during laser irradiation. Whether or not this effect can account for the differences observed in M2 glazed with a laser and electron beam is a subject for continuing research.

3.2 Morphologies in M42 and M7; Alloying effects

As has been indicated in the previous section the carbon con-

tent of highly alloyed* tool steels can be critical in determining the complexity of the solidification route. The analyses of M2, M42 and M7 are given in Table I. The M42 differs from M2 in carbon content, 1.09wt% versus 0.84wt%, in cobalt content, 7.88wt% versus 0.13wt%, and in "tungsten equivalent", 20.6wt% versus 16.22wt%. The "tungsten equivalent" (W+2xMo) to carbon ratio is kept constant however. M7 differs from M2 in a similar manner notably carbon, 1.01wt%, and Mo/W ratio, with the "tungsten equivalent" to carbon ratio also held constant.

The M42 and M7 tool steels are thus very similar to M2 in all but carbon content. The high cobalt content of M42 will certainly effect its tempering response however the solidification structures of M42 and M7 are determined in the main by the total tungsten/molybdenum content and the carbon level.

Samples of M42 and M7 were glazed as described in Sect. 2 and the cross sections examined by scanning electron microcopy. The microstructures observed are summarized in Figs. 3 and 4 for M42 and Fig. 5 for M7.

Fig. 3 shows, at increasing magnification the general structure present in M42 tool steel glazed at 100cm.s.$^{-1}$($\dot{T}\sim 5\times10^{6}$deg.C.s.$^{-1}$). The zone is characterized by a segregation structure superimposed on an otherwise homogeneous solidification pattern of cellular dendrites surrounded by a carbide network. The abrupt changes in solidification pattern observed in M2, Figs. 1 and 2, are absent in M42 however the pronounced segregation pattern follows closely the maps of convection

*See Appendix II

and turbulence that exists in electron beam welds, Fig. 1(d), (e) (8). EDAX analysis of the compositional variations within the zone show clearly that the heavy elemental carbide formers Mo and W are involved ir the segregation bands, Fig. 6(a). The appearance of fluid flow induced segregation of heavy elements in the quenched zone occurs when the local solidification time is shorter than any time required to homogenize by the diffusion of Mo/W and/or their carbides in the liquid state. Fig. 4, M42 glazed at 25cm.s.$^{-1}$($T\sim10^{5}$deg.C.s.$^{-1}$), by contrast has far fewer prominent segregation bands. This is to be expected on the basis of longer local solidification times (lower cooling rate) at this glazing speed, allowing more time for solute diffusion, and it is indeed borne out by the EDAX map for Mo shown in Fig. 6(b). The general solidification structure shown in Fig. 4, a carbide network surrounding cellular dendrites, is similar to that depicted for the high cooling rate sample, Fig. 3, although on a coarser scale. These trends were maintained for all the M42 samples examined--the lower the cooling rate the less segretated the zone and the coarser the microstructure. The "frozen in" segregation is thus limited to the high cooling rate samples that experience short local solidification times throughout the melt zone and to the melt zone edges in other samples where the initial solidification rate is expected to be high.

Unlike M2, and similar to M42, M7 responds to electron beam glazing by solidifying to an even etching zone. Fig. 5 shows an M7 zone glazed at 50cm.s.$^{-1}$($T\sim10^{6}$deg.C.s.$^{-1}$). Microstructurally it is similar to M42 containing typical cellular dendrites. There is some evidence of convection induced segregation in all M7 zones, but it is not so exaggerated as in Fig. 3. However, in the more rapidly solidified M7 zone

the turbulent flow of melt along the lower zone/parent interface produces a segregation pattern that is "frozen in", Fig. 5.

From equilibrium phase diagram considerations it is expected that both M7 and M42 will first solidify to form austenite since the carbon content is greater than the peritectic limit. This is in fact observed. Both M7 and M42 exhibit a microhardness typical of a martensite matrix with a fraction of retained austenite and etch accordingly. It is interesting however that even given the segregation visible in Fig. 3 the solidification mode is stable. It is clear that the precise solidification route is very sensitive to carbon content and that the extra carbon present in M7 and M42 stablizes the formation of austenite from the liquid. The result of this stabilization is that even given local compositional variations the electron beam glazed zones are essentially martensitic with a greater or lesser extent of retained austenite.

4. TEMPERED MICROSTRUCTURES AND ASSOCIATED MICROHARDNESS OF ELECTRON-BEAM GLAZED MATERIALS.

4.1 Tempering characteristics of M2 alloy

(a) Microstructure. As noted in previous studies on laser and electron beam glazed material martensite is not observable in the optical and scanning electron microscope, either in the as-glazed or subsequently heat treated condition. Serendipitously, the formation of discernable tempered martensite plates in glazed M2 was noted in studies of surface layers produced by a scanning electron beam. see Fig. 7. This finding showed, that unlike M42 and M7, tempered martensite in glazed M2 forms at an appreciable rate, a fact confirmed by heat treating a single-pass glazed specimen for only 5 mins. at 560°C. The progressive development of this structure during tempering at 560°C is

such that a highly dense and homogeneous condition is attained within one hour. In this fully transformed condition individual martensite plates are no longer discernable, even after heavy etching in Vilellas reagent.

This study shows that the effect of alloy chemistry on post-glazing heat treatment is quite graphic. For instance, in the alloy with the increased amount of carbon and the cobalt addition (M42) the transformation of the glazed zone to martensite is much slower (see a later section). This behavior is fortunate from an experimental point of view since the progressive increase in the amount of martensite with tempering is observable under well controlled conditions, see Figs. 8-10.

(b) Microhardness. Microhardness values for M2 glazed material, as a function of tempering treatment at 560°C, are plotted in Fig. 8 for specimens glazed with a beam velocity of 100, 50, 25, and 10cm.s^{-1}; data for an unglazed specimen is included for reference. The four tempering treatments consisted of a (i) single temper for 5 mins., (ii) single temper for 1 1/2 hours, (iii) double temper, 1 1/2 hours followed by a further 1 hr., and (iv) triple temper, 1 1/2 hours followed by two 1 hour tempers. As already noted two distinct phase regions exist within glazed zone of M2 steel, namely the light-etching γ/α' regions and the dark δ-ferrite regions. The microhardness measurements herein cited are for the γ/α' phase regions.

A noteworthy feature in Fig. 11 is the pronounced shift of the secondary hardening peak towards a longer time and higher hardness for the three rapidly solidified zones. In these specimens (glazed at 100, 50, and 25 cm.s^{-1}) the time for attaining maximum tempered hardness is doubled, i.e. 2 hours, as compared with 1 hour in conventionally treated material. Furthermore, the maximum attainable hardness, appears from

limited results, to increase with increasing glazing speed. The enhanced tempering characteristics just considered naturally reflect a carbide dispersion in which the (i) phase(s), (ii) particle size, and (iii) distribution favor an increase in strength and stability. Quite apart from the significant refinement in carbide particle distribution, it is pertinent to note that the nature and relative amount of carbide phase precipitation during heat treatment differed significantly in prior-glazed material. For instance M_2C carbide is present to a much greater degree than in conventionally treated material, and M_6C was not identified. Elucidation of the precise nature of carbide distributions resulting in the enhanced tempering characteristics shown in Fig. 11 is an important area for further study.

Another aspect of the effect of glazing-rate is also seen in Fig. 11 for the material glazed with significant beam penetration (beam velocity = 10 cm.s.$^{-1}$). In this case the solidification note is relatively low ($\sim 5 \times 10^4$ deg.C.s.$^{-1}$) and, in addition, the slower cooling rate in the solid state is important in carbide precipitation reactions. As seen in Fig. 8, the maximum tempered hardness is obtained after single tempering for one hour; additional treatment beyond this is clearly detrimental. Differences in the secondary hardening peak position as a function of the glazing velocity reflects the effect of cooling rate on the scale of the finely dispersed carbide distribution. It should be emphasized that the cooling rate during (i) solidification and (ii) solid state heat dissipation are equally important. The nature of the carbide morphology and the homogeneity of the alloying elements does, in turn, determine the subsequent tempering characteristics. Presumably, the rapidity of attaining the maximum tempered hardness in the slowly

glazed material is a result of a well developed carbide distribution during electron-beam processing.

Finally, as shown in Fig. 11 the results obtained by short-term tempering (5 minutes) follow no simply defined trend. The variations in as-quenched hardness however are likely to arise from differing δ-ferrite and retained austenite content. Thus the changes in hardness that occur on 5 minute tempering may well reflect changes in the martensite content brough about by further tranformation of $\gamma \rightarrow \alpha'$. The prior existing α' will of course now etch to reveal the typical tempered martensite structure. Clearly a careful study of short-term tempering is highly relevant in view of the inherent tempering that results from residual heating during surface area glazing.

4.2 The Tempering Characteristics of M42 & M7

(i) Microstructures. The comparative tempering behavior of glazed M42, M7 and M2 clearly shows the effect of alloying chemistry in modifying the time required for forming (i) tempered martensite, and (ii) secondary hardening peak carbide precipitates. In contrast to M2, martensite plates are clearly discernable in all glazed material after tempering at 538°C. It is well evident in Fig. 8 that the density and scale of the martensite plates is very sensitive to the glazing velocity. At the highest glazing velocity (100 $cm.s.^{-1}$) the amount of martensite (α') is, in fact, relatively small so that untransformed austenite (γ) is the predominent phase. As found in M2, the as-glazed phases are particularly resistant to chemical attack (by Vilellas reagent and other etchants) so that the solidification structure is not revealed.

A dominent feature of the thin martensite plates in Fig. 9a is that their length (20 to 30μm) is significantly greater than that of the martensite within conventionally treated (parent) material. This is a

consequence of a relatively large austenite grain size formed during the rapid solidification process. In contrast, it should be noted, the actual solidification cellular (or dendritic) structure, unlike the grain size, exists on an ultra-refined scale.

An intriguing feature of the zone in Fig. 8(a) is that the distribution pattern of the tempered martensite resembles the segregation pattern resulting from convective and turbulent liquid flow within the solidifying melt zone, see Fig. 1 in the previous section. Thus, we see that the segregated regions of specific alloying elements (namely Mo and W) persist, at least to some extent, throughout the first tempering treatment. Associated with the concentration variation of these elements there is, in consequence, a localized variation in the kinetics for tempered martensite formation during heat treatment.

Comparison of Figs. 8a, b, and c shows the systematic way in which reducing the glazing velocity increases the proportion, degree of refinement, and homogeneity of the martensite in the tempered structure. At the lowest glazing velocity (10 $cm.s^{-1}$) the majority of austenite has been transformed to produce a fairly homogeneous martensitic microstructure after the one hour tempering treatment. As prviously discussed, the Mo and W segregation patterns produced by convection and turbulent flow became less distinctive with decreasing glazing velocity and not in evidence in the zone glazed at 10 $cm.s^{-1}$. With a zone of homogeneous chemical composition (such as the one seen in Fig. 8c, where $v=10cm.s^{-1}$) the kinetics for martensite formation will be reasonably isotropic.

From a fundamental point of view it is of interest to know if the martensite plate length is a function of cooling rate during the initial glazing process. At first glance, it appears from Fig. 8 that the plate

length progressively decreases with decreasing glazing velocity. This general visual impression however, may be deceptive, since in Fig. 8a the individual martensite plates are clearly discernable, whereas in Fig. 8c. they are densely crowded together. It is possible, for instance that the microstructure in Fig. 8c. first developed by the nucleation and growth of long martensite plates within the austenite. Then by the progressive development of the martensitic structure the mean plate length is gradually reduced simply by the nature of the problem of geometrical "crowding."

As would be anticipated the $\gamma \rightarrow \alpha'$ transformation is nearer completion following a double tempering treatment at 538°C. The difference between single and double tempering is particularly pronounced in material glazed at the highest rate of 100 $cm.s.^{-1}$; this is seen by comparing Figs. 8a. and 9a. In Fig. 9a., however, there are still small regions where the higher content of Mo and W has supressed the martensite formation. Another feature in double tempered material is individual martensite plates cannot be discerned when the retained $\gamma \rightarrow \alpha'$ transformation has proceeded to a considerable degree. Within the "featureless" martensitic structure the original dendritic solidification structure is now discernable upon etching with Vilellas reagent, see Fig. 9b.

Effects of alloy chemistry on tempering characteristics are well known (e.g. (11)) and one might anticipate that the relatively large addition (8wt%) of cobalt in M42 significantly effects the tempering characteristics of rapidly solidified material. The cobalt addition in conventionally treated material, it should be noted, is to improve hot hardness. In the present results, however, the tempering character-

istics of glazed M42 are rather similar to those of M7, an alloy whose only significant compositional difference is the absence of cobalt.

In summarizing findings on M7 it should be noted that, as in M42, the observations indicate that austenite forms directly from the melt and not via a peritectic reaction. Fig. 10 shows a set of progressively increasing magnification micrographs from a M7 specimen originally glazed at 50 $cm.s.^{-1}$ and single tempered at 538°C for 1 1/2 hours. In contrast to M42, the microstructural features arising from convective flow segregation are more readily apparent in the tempered condition than immediately after glazing. The darkly etching regions in Fig. 10a are obviously reminiscent of those seen within the convective flow paths in Fig. 1d. As previously observed in M42 the martensite plates in M7 are significantly longer than in the parent material. Typically, they are $\sim$20μm in length (see Fig. 10 b and c) and unaffected by the fine-scale dendritic solidification structure; they are also, unimpeded by fine carbide particles.

In the microhardness vs. tempering time curves for M42 and M7 (see Figs. 12 and 13) the double tempered hardness is seen to exceed that in conventionally processed material provided the glazing velocity is sufficiently high. For the alloy M42 (see Fig. 12) the optimum tempered hardness is (i) inferior and (ii) comparable to that of conventionally processed material when the glazing velocity is respectively 10 and 25 $cm.s.^{-1}$. When, however, the glazing process is carried out at higher velocities (50 and 100 $cm.s.^{-1}$), thus imposing a higher cooling rate, the double tempered hardness exceeds that obtained by conventional processing. Quite clearly, the curves in Fig. 12 for material glazed at 50 and 100 $cm.s.^{-1}$ are incomplete since the actual peak would appear to occur for a longer tempering time, possibily after triple tempering (as

is the case for M2, see Fig. 11). As is evident from Fig. 13 the tempering behavior for M7 is rather similar to that just described for M42. In this case the amount of tempering is insufficient to produce a secondary hardening peak for material initially glazed at 25, 50 and 100 $cm.s.^{-1}$.

A significant finding revealed in the present study is that electron beam glazed material, processed at a sufficiently high cooling rate, tempers more slowly than that of conventionally hardened material. The similar tempering behavior of M7 and M42 is interesting since this suggests that the level of cobalt addition in M42 could be reduced and, by using electron beam glazing, retain acceptable properties. Obviously this is significant technologically and in the reduction of the cost of improved performance high speed steels.

Effect of Post Austenitization Treatment

There is a distinction between the morphological changes which occur during high temperature heat treatment (at ~1200°C) in (i) electron beam glazed and (ii) conventionally processed high speed steels. In standard practice, particles of various carbide phases either undergo partial or full dissolution during austenization. However, in glazed material high temperature heat treatment results in fine scale carbide precipitation from the initially highly homogenized material. Examples of fine scale carbide particle dispersions in M42 produced by heating prior glazed specimens at 1190°C for 5 minutes are seen in Figs. 14 and 15. The region in Fig. 14 is at the bottom of a zone formed by glazing at a beam velocity of 100 $cm.s.^{-1}$. Within the inhomogeneous carbide dispersion seen in Fig. 14 there are clearly highly concentrated carbide distributions which reveal the segregation bands formed by turbulent flow during electron beam processing. As previously discussed liquid

flow induced segregation diminishes with decreasing glazing velocity so that in Fig. 15 where the glazing velocity is only 10 cm.s.$^{-1}$ the effect is not discernable at all. However an interesting feature of the carbide distribution in Fig. 15 is a preferentially alignment along the dendrites.

A most important feature in austenitized and quenched specimens of M42 is a particularly high microhardness. Specifically, this is 970±23 D.P.N. for the mircrostructure in Fig. 14 and even higher (1158±22 D.P.N.) for the microstructure in Fig. 15. At present the amount of martensite within the zones in Figs. 14 and 15 is unknown since in its austenitized and untempered state it cannot be selectively etched for metallographic examination. In future continuing studies tempering experiments will be conducted and following these the amount of martensite will then be determined. A particularly important aspect of these experiments will be to ascertain if the particularly high microhardness values of 1000 to 1200 D.P.N. are maintained following tempering treatment.

REFERENCES

1. F. Heisterkamp and S. R. Keown, Processing and Properties of High Speed Tool Steel, AIME, Feb. 1980, The Metallurgical Society of AIME.
2. L. Norstrom, Doctoral Dissertation 3891, University of Uppsala, Sweden, (1976).
3. F. B. Pickering and T. Gladman, Metallurgical Developments in Carbon Steels, Special Report 81, p. 10, Iron and Steel Institute, London (1963).
4. T. Minemura, A. Inoue, Y. Kojima and T. Matsumoto, Met. Trans. A, 11A, 671 (April, 1980).
5. P. R. Strutt, H. Nowotny, M. Tuli and B. H. Kear, Mat. Sci. Eng. 36, 217, (1978).
6. Young-Won Kim, P. R. Strutt and H. Nowotny, Met. Trans. A, 10A, 881 (July 1979).
7. J. J. Rayment and B. Cantor, Metal Science 12, 156 (1978).
8. P. R. Strutt, A Comparative Study of Electron Beam and Laser Melting of M2 Tool Steel, Mat. Sci. Eng. 44, 239 (1980).
9. B. G. Lewis, D. A. Gilbert and P. R. Strutt, Processing and Properties of High Speed Tool Steels, p. 84, Ed. M. G. H. Wells and L. W. Lherbier, The Metallurgical Society of AIME (1980).
10. R. Mehrabian, S. Kou, S. C. Hsu and A. Munitz in Laser-Solid Interactions and Laser Processing, pg. 129, American Institute of Physics, 1978.
11. R. W. K. Honeycombe, Structure and Strength of Alloy Steels, Climax Molybdenum Co. Ltd. Publication, Villiers House, 41/47 Strand, London WC2N 5JS.

APPENDIX I

Tempering Tool Steels

The tempering of high speed tool steels is extremely complex and goes beyond the main reason for tempering low alloy steels namely to reduce residual stresses. Some of the common features of tempering, however, are given below.

In the range 25°C-200°C, tempering causes martensite to decompose to a metastable ε carbide $(Fe,M)_{2-3}C$, where M is other substitutional elements in the carbide. This stage has little effect on tool steel hardness. From 200°C and up, $(Fe,M)_3C$ precipitates from the martensite. At the lower temperature end the carbides are needle like, at the higher end spherical. The relatively coarse carbides formed at this stage cause the hardness to decrease. The rate of decrease is slowed by the addition of chromium. The next stage sees the strong carbide forming elements (Mo, W, V) replace the coarse carbides with a fine dispersion of precipitates ($M_{23}C_6$, W_2C, Mo_2C and VC). This brings about an increase in hardness (secondary hardening) until at the higher end of tempering temperature (and time), coarsening of these precipitates causes softening again.

The decomposition of retained austenite takes place over the whole temperature range if time is sufficient. The transformation is generally $\gamma \rightarrow$primary carbides + bainite (low temperatures) and $\gamma \rightarrow$primary carbides + pearlite (in the higher temperature range). These carbides that form on tempering are richer in carbon and e.g. chromium than the retained austenite from which they were transformed. The austenite therefore is lower in these elements near to the carbides and hence has an increased Ms and Mf. Upon cooling this austenite forms fresh mar-

tensite that increases the hardness. In such cases, the retained austenite contributes to the secondary hardening. The fresh martensite also requires tempering which in turn will generate further martensite until all the retained austenite is transformed.

APPENDIX II

Alloy Elements in Tool Steels

The major alloying elements in high speed steels are carbon, chromium, tungsten, molybdenum, vanadium and cobalt.

Carbon

Carbon levels in the range 0.7% (T1) to about 1.6% (T-15) are found in tool steels, Its function is to provide high as quenched hardness (high carbon martensite), large wear resistant carbides, and the source of carbon for precipitation carbides during secondary hardening.

Chromium

Chromium is used in all high speed steels (3.5-4.5%) as an aid to hardenability, to form large wear resistant carbides and for its corrosion resistance (prevents scaling to some degree).

Tungsten

Tungsten is used in most high speed steels, 12-19% in T-steels, 0.5%-7% in M-steels. The presence of tungsten helps promote hot hardness, forming wear resistant carbides and contributes to secondary hardening via the formation of W_2C precipitates.

Molybdenum

Molybdenum is used in many steels including of course all of the M-type steels (4-10%). Molybdenum has the same effect as tungsten - being interchangeable except that 1wt%Mo ≡ 2wt%W.

Vandium

Vanadium again is in all tool steels (1-5%). It forms a highly wear resistant carbide, VC, which is the hardest found in the tool steels. These carbides help maintain fine grain size during elevated temperature heat treatments.

Cobalt

Cobalt is used in the range 0-12% to give a high hot hardness by retarding the breakdown of martensite at elevated temperatures.

FIGURE CAPTIONS

Fig. 1 Schematic diagram showing the phase distribution in laser glazed M2 (a) and electron beam glazed M2 (b), (c). Also shown schematic are convective flow paths in molten zones (d), (e).

Fig. 2 (a),(b) Two as solidified zones in electron-beam glazed M2. The phase distributions are similar to those depicted in Fig. 1 (b) and (c) respectively and are related to the convection currents in the molten zone. (see text)

Fig. 3 SEM micrographs of the as-glazed structure in M42--glazing velocity 100 $cm.s.^{-1}$.

Fig. 4 SEM micrographs of the as-glazed structure in M42--glazing velocity 25 $cm.s.^{-1}$.

Fig. 5 SEM micrographs of the as-glazed structure in M7--glazing velocity 50 $cm.s.^{-1}$.

Fig. 6 (a) EDAX X-ray map for Mo in M42 glazed at 100 $cm.s.^{-1}$.
(b) EDAX X-ray map for Mo in M42 glazed at 25 $cm.s.^{-1}$.

Fig. 7 Martensite plates in surface glazed M2. (Mag x130)

Fig. 8 Single tempered microstructure in M42 originally glazed at
(a) 100 $cm.s.^{-1}$
(b) 25 $cm.s.^{-1}$
(c) 10 $cm.s.^{-1}$

Fig. 9 Double tempered microstructure in M42 originally glazed at
(a) 100 cm.s.$^{-1}$
(b) 25 cm.s.$^{-1}$

Fig. 10 (a)-(c) Progressively increasing magnification SEM micrographs of single tempered M7 originally glazed at 50 cm.s.$^{-1}$.

Fig. 11-13 Tempering response for, in order, M2, M42 and M7. Microhardness (DPN, 50 gm. load) is plotted as a function of tempering treatment. (Sample #1-4 refer to glazing velocity--100, 50, 25 and 10 cm.s.$^{-1}$ respectively).

Fig. 14 SEM micrograph of M42 zone re-austenitized at 1190° for 5 minutes. Original glazing speed was 100 cm.s.$^{-1}$.

Fig. 15 SEM micrograph of M42 zone re-austenitized at 1190° for 5 minutes. Original glazing speed was 10 cm.s.$^{-1}$.

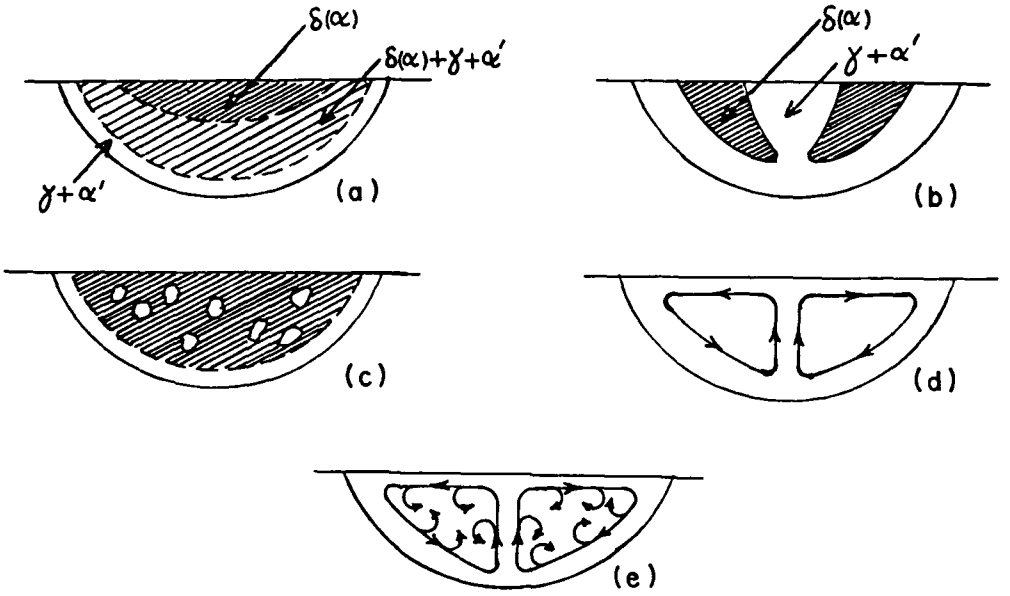

Fig.1

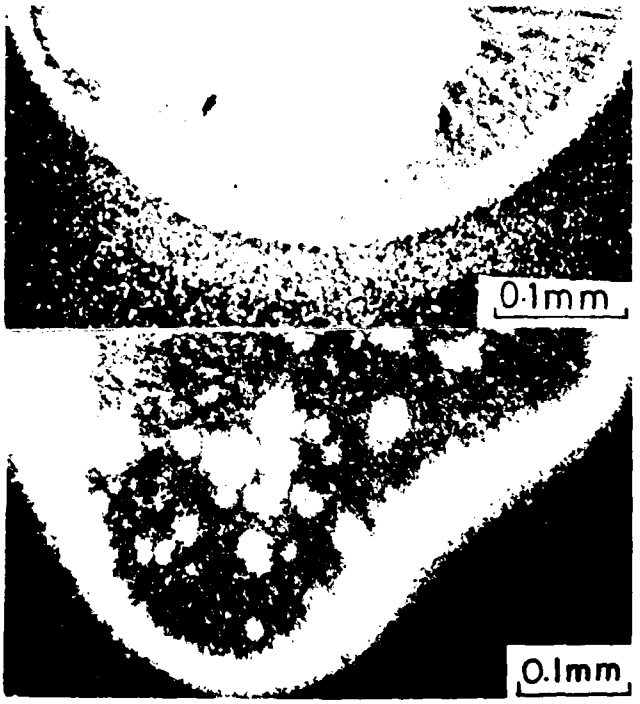

Fig . 2

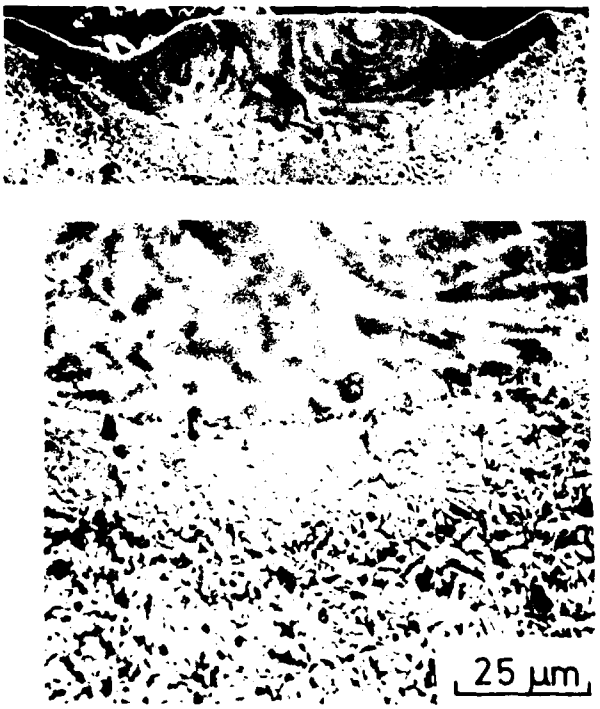

Fig . 3

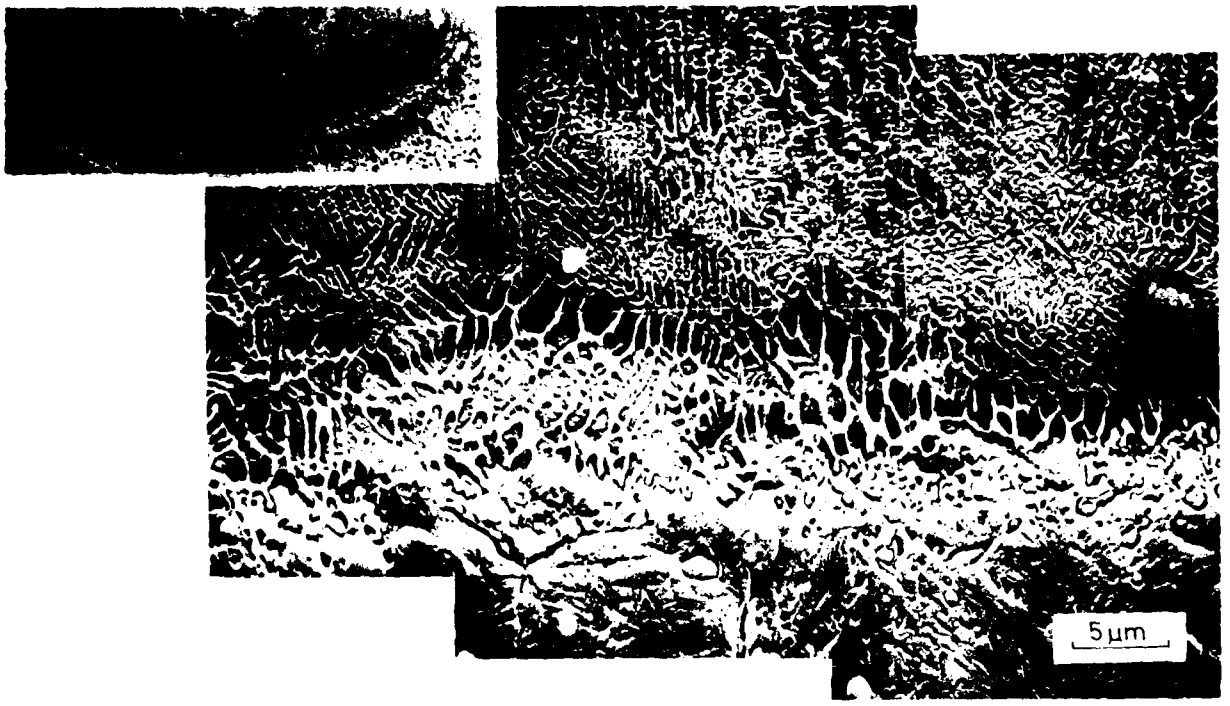

Fig. 4

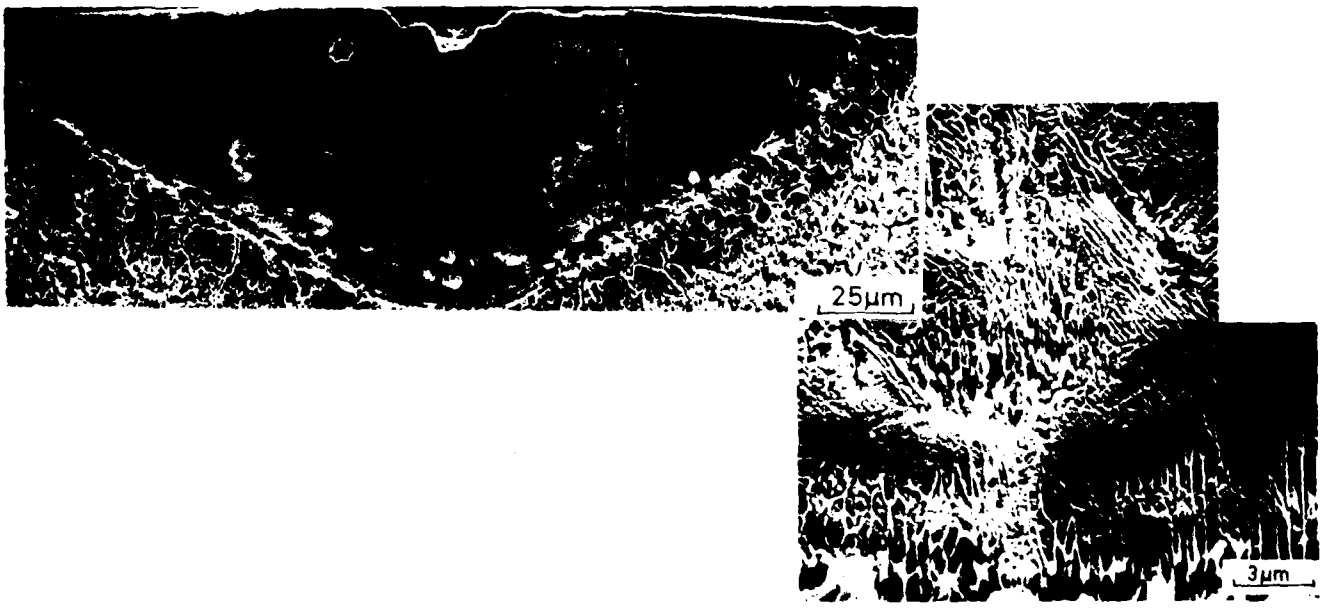

Fig. 5

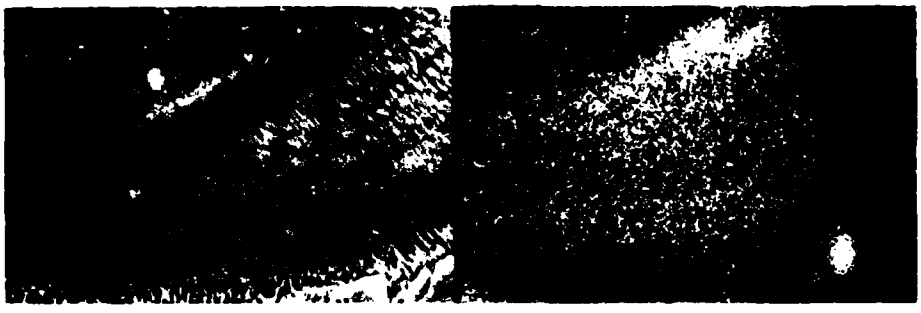

(a)

(b)

Fig.6

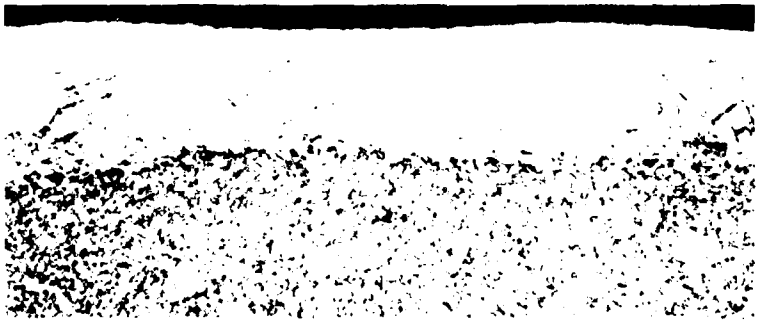

Fig.7

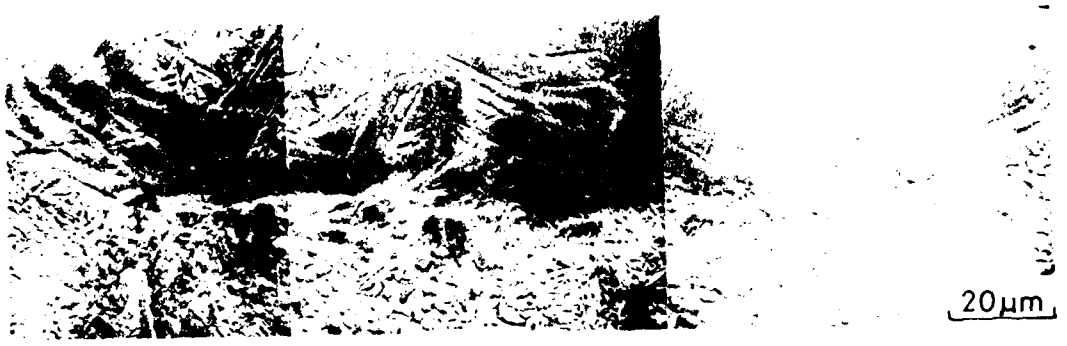

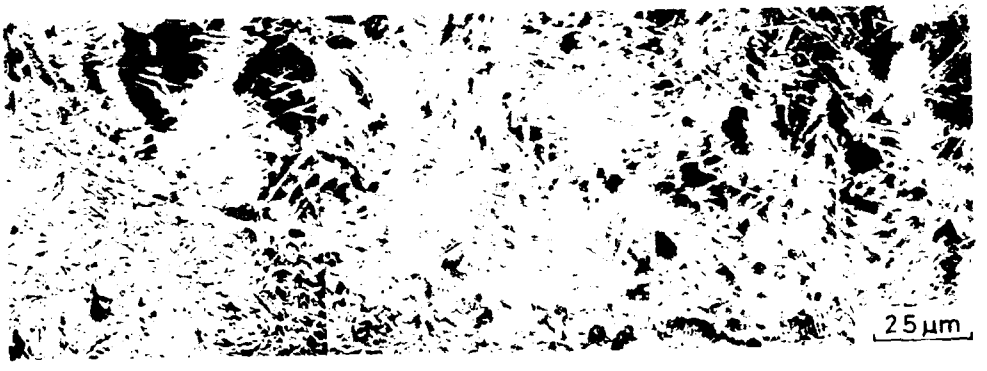

Fig. 8

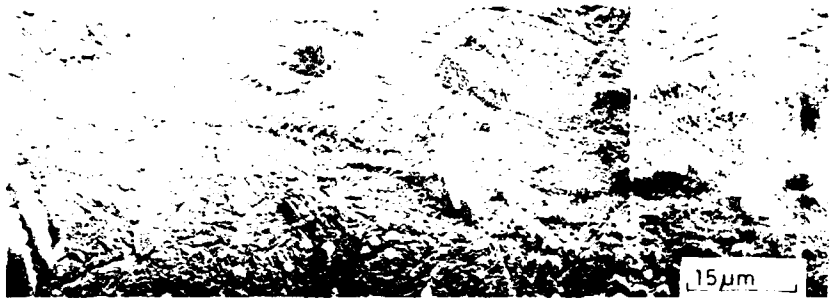

(a)

(b)

Fig .9

(a)

(b)

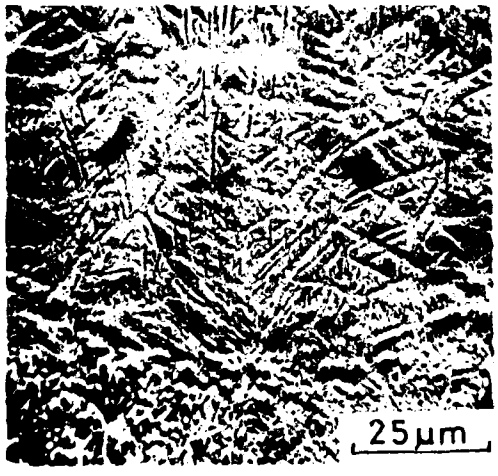

(c)

Fig .10

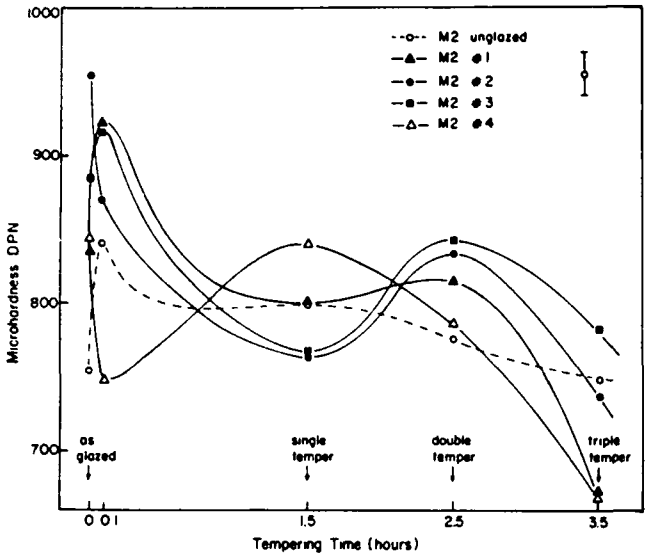

Fig .11

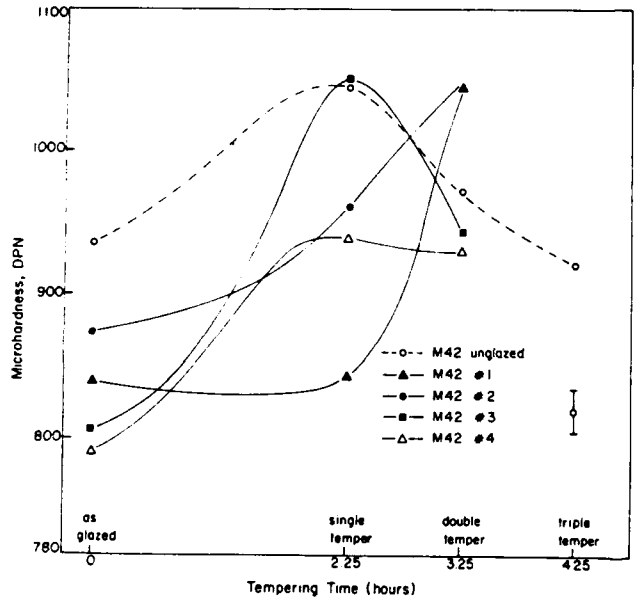

Fig .12

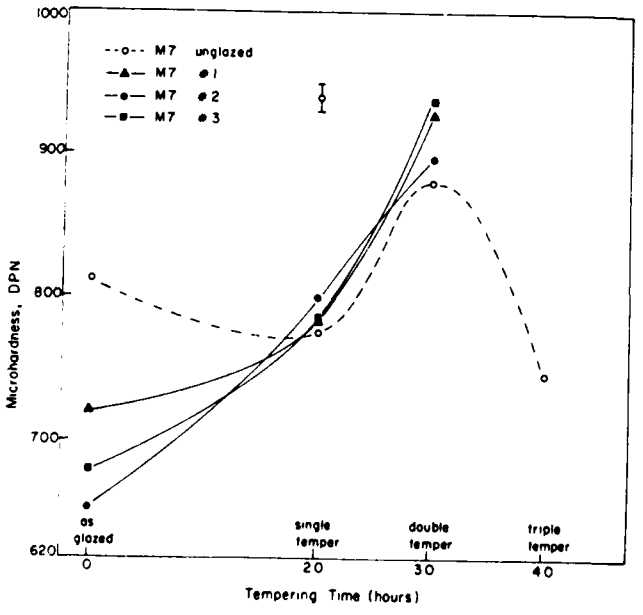

Fig .13

Fig.14

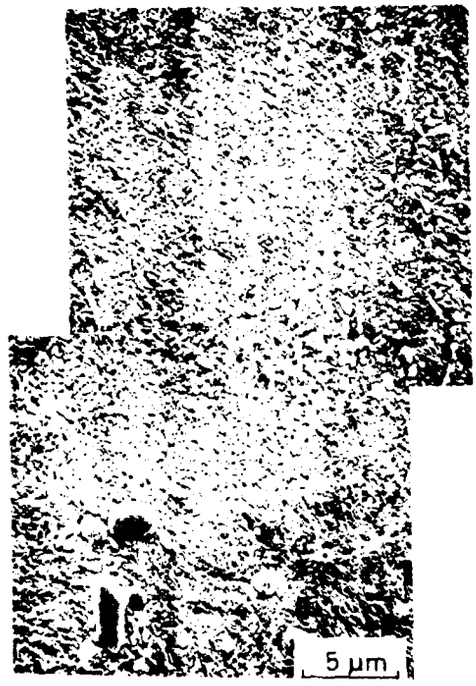

Fig.15

SECTION 4

TRANSMISSION ELECTRON MICROSCOPE STUDIES

TRANSMISSION ELECTRON MICROSCOPE STUDIES

Transmission electron microscope observations together with optical and scanning electron microscope observations provide an overall view of the microstructural characteristics of laser and electron beam glazed material. A particular difficulty, however, is in obtaining satisfactory thin foil specimens due to the markedly different electrochemical characteristics of glazed and unglazed steel. In M2 tool steel, for example, glazed material is particularly resistant to chemical and electrochemical attack. Thus, in a ϕ2.3mm disc sample with a single 0.25 to 0.5 mm width zone perforation during thinning invariably occurs with the surrounding unglazed material unless particularly careful procedures are adopted. As might be anticipated thin foil preparation is greatly facilitated if the melt zone is reasonably wide and the results now presented were obtained in such a zone using a 0.5 $cm.s^{-1}$ beam velocity. These deep penetration zones were formed using a beam power of 375 watts and the cooling rate is estimated to be $\sim 2 \times 10^3$ $degC.s.^{-1}$.

Thin foil specimens were examined from electron beam glazed M2 tool steel and 52100 steel. First we consider the results obtained with the tool steel. In Fig. 1 the cell boundaries formed during solidification are discernable and measurements from several samples show that the mean grain size is $\sim 3\mu m$. Microtwinning, which analysis showed to occur on {112} planes, is also seen in Fig. 1, and more clearly in the higher magnification micrograph in Fig. 2. The microtwin thickness was found to vary from 400 A^{o} to 1800 A^{o} and in the case of particularly refining microtwinning there was noticeable streaking of twin spots in the diffraction pattern. Frequently, a grain was found to be divided into distinct regions, each of which displayed microtwinning on a particular set of {112} planes. Such regions, as may be seen in Fig. 2, are not deduced

to be martensite packets of the type described in Fe-Ni alloys (1). This conclusion is based on optical and scanning electron microscope observation unambiguously showing that martensite plates extending through several grains have a closely related crystallographic orientation.

The schematic diagram in Fig. 3 shows the diffraction pattern corresponding to the foil orientation and specific type of twin orientation in Figs. 1 and 2. Although twinning is readily discernable in the M2 tool steel martensitic structure, the total volume of twinned material cannot be significant. This conclusion is based on the fact that the actual twin diffraction spots are generally weak, so also are the double diffraction spots. In the 52100 steel, however, this is not the case and one thus concludes that the degree of microtwinning in martensite in rapidly quenched steels is composition dependent.

C. S. Roberts et al. (2) have pointed out that for X-ray powder pattern work there are no reliable data on the tetragonality of martensites with less than about 0.6% carbon because of the broadness of the diffraction lines and the merging of the doublets. Employing a single-crystal X-ray technique, they successfully identified that the low carbon martensite is tetragonal with an axial ratio corresponding to a carbon content of 0.25%. Sare et al. (3) did not observe tetragonality in water-quenched filings of M1 high-speed steel using X-ray powder diffraction analysis, in agreement with Cohen's findings. Cantor et al. (4) also failed to detect tetragonality in as-quenched X-ray diffractograms of splat-cooled M42, M2 and T1 steels. As discussed by the latter authors, however, this is not conclusive because the peaks are relatively broad due to a distribution of cooling rate dependent solubility limits, small grain size and the existence of internal strain. Sare et al. also reported that no tetragonality was evident in the martensite reflections in the both splat-cooled alloys and water quenched filings of iron-molybdenum-carbon alloys (5)

and iron-titanium-carbon alloys (6).

In contrast to the findings discussed above there is clear evidence that tetragonality is detectable, and indeed measurable, in electron beam glazed material. The amount of tetragonality is determined by careful measurement of distances and angles in diffraction patterns, see Fig. 4. As a result of the non-unity c/a value the lengths of the $\bar{g}_1$ and $\bar{g}_2$ vectors differ slightly with corresponding d spacing values of 1.193 and 1.171 Å; the angular difference between α_1 and α_2 is 3.6°. From these values of the reciprocal vector lengths and the included angles α_1 and α_2 (see Fig. 4) and the c/a ratio is 1.038. On the basis of the experimentally established relation between c/a and carbon concentration the material is deduced to have a carbon content of 0.85wt%, i.e. the nominal value.

The structure of the quenched zones of M2 has also previously been investigated by powder x-ray diffraction (7) and in these experiments indeed no tetragonality (of the α phase) was observed in the powder pattern. However recent X-ray diffractograms from electron beam glazed zones of similar dimensions to those used in the TEM work have been obtained by removing the quenched region by spark machining and carrying out <u>bulk</u> X-ray analysis on the extracted sample. Under these conditions a small degree of tetragonality was observed corresponding to martensite lattice parameters of $a=2.88\pm0.05$Å, $c=2.91\pm0.05$Å$(c/a\simeq1.01)$. As mentioned above the expected tetragonality (c/a) for martensite in M2 tool steel is $\sim$1.04 assuming that all the carbon is held in solution and not precipitated in the form of carbides. The difference between the X-ray and TEM results is not altogether unexpected both from X-ray line broadening considerations (2) and from the fact that the X-ray analysis reflects an averaged result while the TEM diffraction patterns are from local (10-20 μm) regions.

It is worth discussing briefly further data concerning the tetragonality determinations. Fig. 5(a), (b) shows a backscattered electron image of a relatively shallow glazed M2 zone together with a wavelength dispersive X-ray (WDX) mapping of carbon. The carbon is apparently concentrated in the deep (dark) etching regions of the zone and beyond the melt zone/parent boundary. The carbon segregation within the melt zone is difficult to explain. Generally it is expected that austenite will be higher in alloy content than ferrite, yet, here, a reversal of that scheme is observed. The absence of a higher carbon content in the austinite/martensite may explain the low (and often undetectable) degree of tetragonality. It should be noted that the relatively high carbon content of the dark etching ferrite areas arises from the carbide network just visible in Fig. 5(a) and shown at high magnification in Figs. 6(a), (b). It seems possible that the act of light etching prior to WDX analysis leaves the carbides proud of surface and available to absorb and re-emit the matrix X-rays thus enhancing the measured carbon levels. Further careful WDX analysis is currently underway to examine solute distribution in glazed zones.

Returning to TEM analysis of M2, it is interesting to compare the microstructures in Figs. 1 and 2 with that formed at a higher solidification rate, see Fig. 7. This micrograph (Fig. 7) is from a splat-quenched sample of M2 tool steel and as a result of the more rapid quenching the mean grain diameter is 0.3μm; the estimated cooling rate is $\sim 5 \times 10^{6}$ deg.C.s.$^{-1}$. Even in this more refined microstructure, the dominant features are similar to those observed at the lower cooling rate (2×10^{3} deg.C.s.$^{-1}$).

Finally in glazed samples of the high carbon steel 52100 electron microscope observations revealed features somewhat similar to those described for M2. One significant difference, however, was the dominance of microtwinning where twin spots in the diffraction patterns were much stronger than in M2 tool steel.

This was accompanied by a greater intensity of the double diffraction reflections. Measurement of the degree of tetragonality again showed that the estimated carbon concentration corresponded to the nominal value, i.e. 1.0wt%. Another feature was that unlike M2 twinning apparently occurred on one primary set of {112} planes within each grain.

1. F. Duflos and B. Cantor, in "Rapidly Quenched Metals III" edited by b. Cantor (Metal Society, London, 1978) vol. 1, p. 110.
2. C. S. Roberts, B. L. Averbach and M. Cohen, Trans, ASM, 45 (1953), 576.
3. I. R. Sare and R. W. K. Honeycombe, Metal Science, 13 (1979), 269.
4. J. J. Rayment and B. Cantor, Metal Science, 12 (1978), 156.
5. I. R. Sare and R. W. K. Honeybombe, J. Mater. Sci., 13 (1978), 1981.
6. Ibid, Metal Science, 14 (1980), 177.
7. Young-Won Kim, P. R. Strutt and H. Nowotry, Met. Trans. A., 10A, (1979), 881.

FIGURE CAPTIONS

Fig. 1 Transmission electron micrograph of cellular solidification structure in M2 high speed steel, this structure was formed by electron beam melting.

Fig. 2 Twinning within martensite plates in electron beam melted M2 high speed steel.

Fig. 3 Schematic diagram of the diffraction pattern corresponding to the foil orientation in Figs. 1 and 2, showing the martix, twin, and double diffraction reflections.

Fig. 4 Schematic diagram showing slight-distortion of diffraction pattern arising from tetragonality, see text.

Fig. 5 Scanning micrograph of melt zone in M2 high speed steel with the corresponding carbon map obtained with the X-ray wavelength dispersive system.

Fig. 6 Higher magnification scanning micrograph and carbon map of a region within the field of view in Fig. 5.

Fig. 7 Rapid solidification cellular structure in a splat quenched foil of M2 high speed steel.

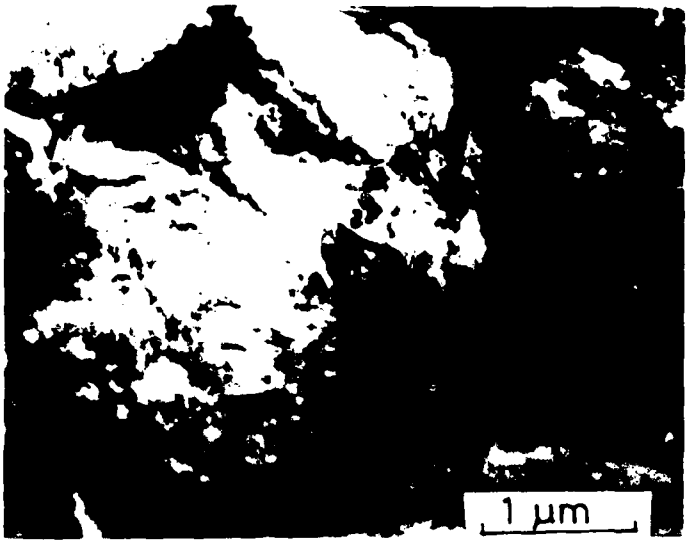

Fig.1

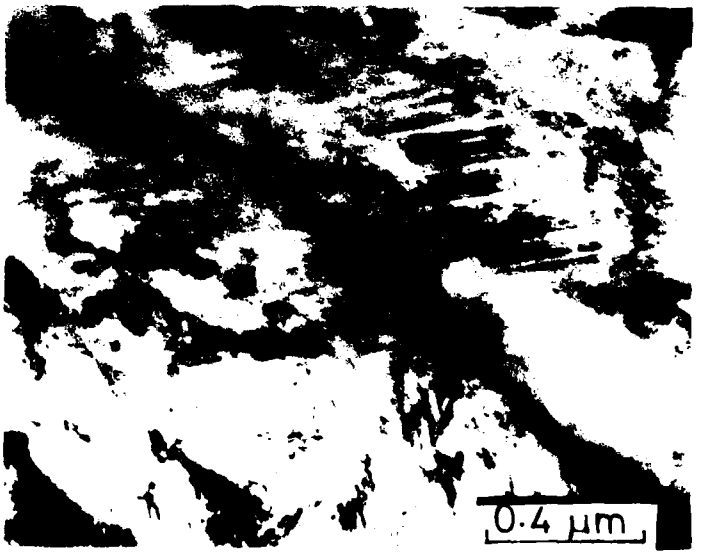

Fig.2

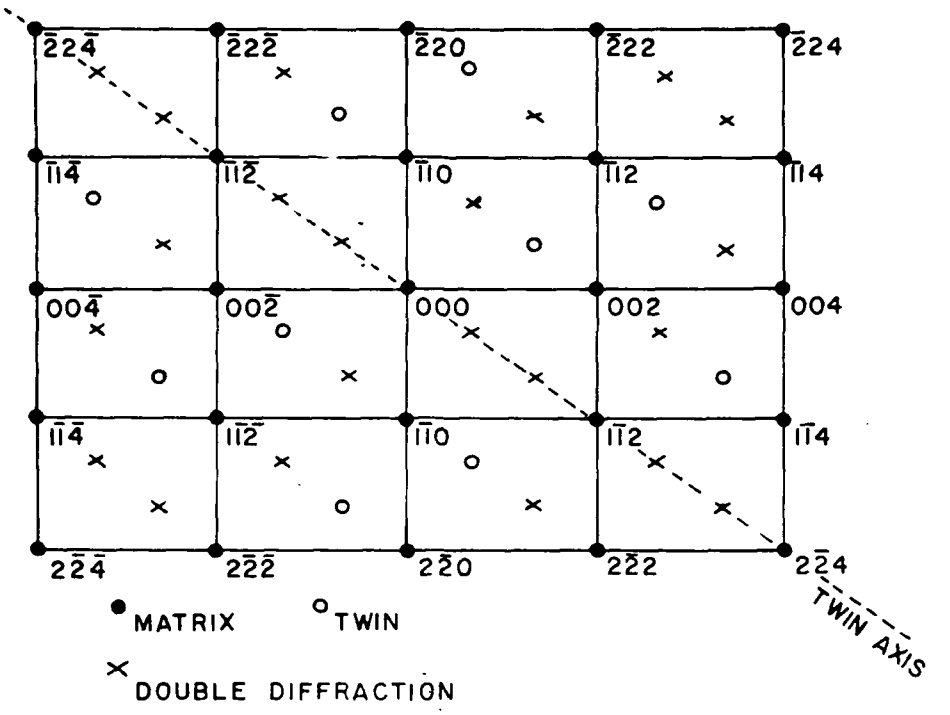

Fig.3

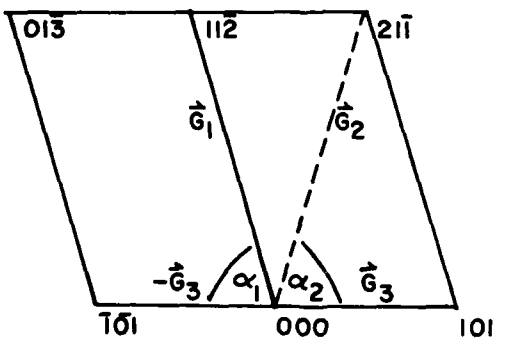

$d_{11\bar{2}} = 1.193A°$, $d_{211} = 1.171A°$, $d_{101} = 2.053A°$.

$\alpha_1 = 75.07°$; $\alpha_2 = 71.50°$.

$c/a = 1.038$.

$[\bar{1}3\bar{1}]$ – Orientation

Fig.4

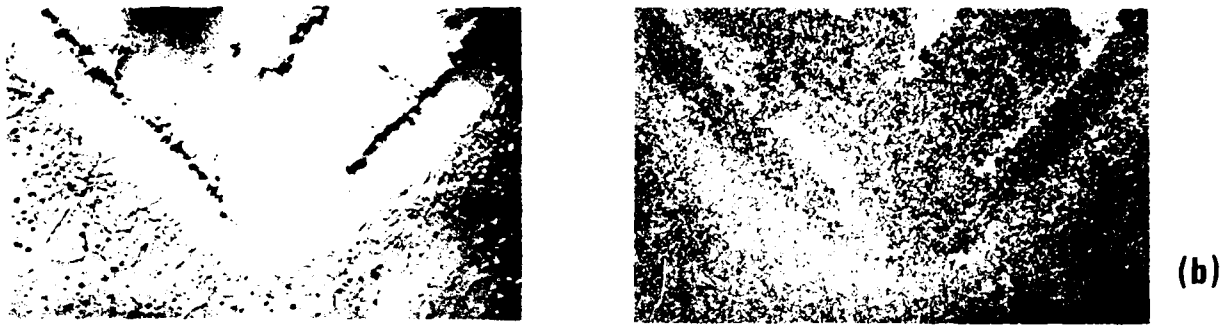

Fig.5

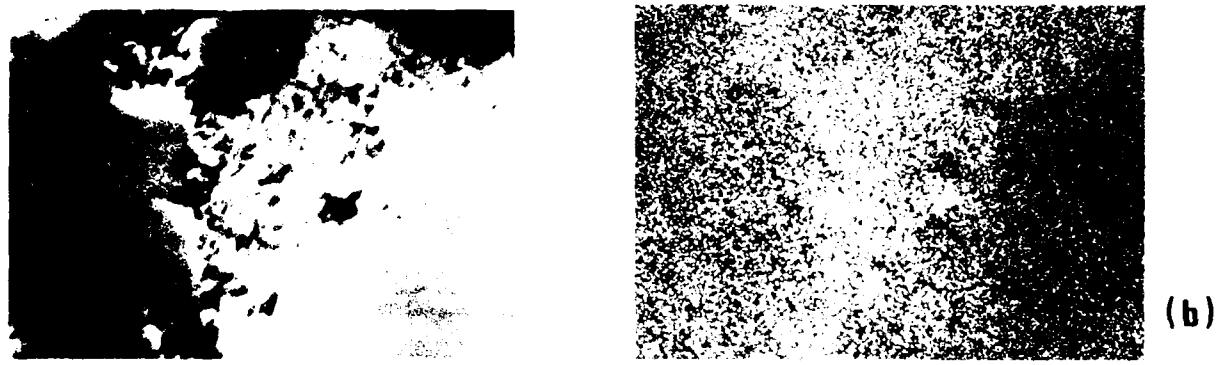

Fig.6

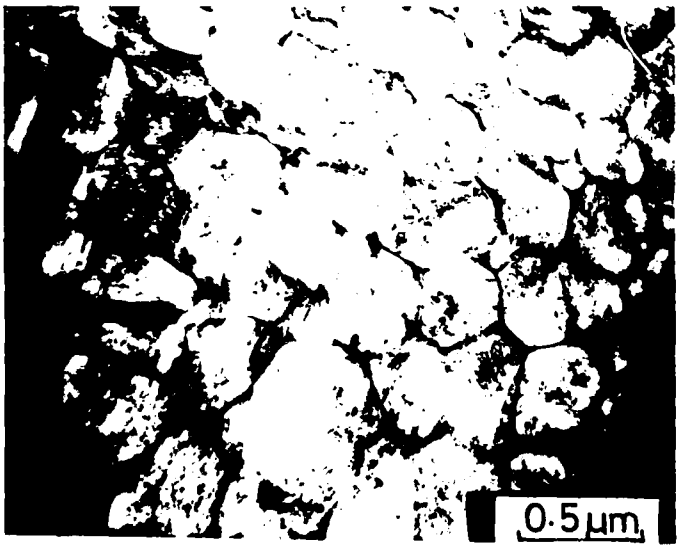

Fig.7

SECTION 5

WEAR CHARACTERISTICS OF AN ELECTRON-BEAM GLAZED IRON-BASE CEMENTED CARBIDE MATERIAL

WEAR CHARACTERISTICS OF AN ELECTRON-BEAM GLAZED IRON-BASE CEMENTED CARBIDE MATERIAL

1. INTRODUCTION

Electron-beam surface area glazing of hard iron-base materials results in enhanced microhardness and microstructural refinement favoring isotropic mechanical properties. These features are naturally important in terms of potential wear applications and initial studies on wear characteristics have yielded encouraging results (1). The materials initially selected (1,2) were the molybdenum base high-speed steel M2 and the "Ferro-Tic" cemented carbide SK. The latter material is based on the pseudo-binary Fe-TiC alloy system, however, alloying additions have been made to form a tool steel matrix; the amount of titanium carbide is ∿36wt%. It has been found that SK and also other "Ferro-Tic" materials resist cracking during electron beam glazing and furthermore undergo marked microstructural refinement. In essence, the large original TiC particles dissolve, due to combined superheating and turbulent stirring during the glazing process, and an ultra-refined microstructure containing primary TiC dendrites forms upon rapid solidification.

The high microhardness and degree of carbide particle refinement in electron-beam glazed "Ferro-Tic" materials is, as stated already, of particular importance in wear applications. In view of this, wear studies on glazed SK material (2) have been extended to examine the reproducibility of wear results and also the effect of wear against a steel counterface material of a (i) moderate and (ii) high hardness.

2. EXPERIMENTAL RESULTS

2.1. Heat Treatment and Wear Testing

All the material used, whether it was subsequently wear tested in the (i) glazed or (ii) unglazed state was initially austenitized at 1050°C for 5 mins. and then quenched into warm oil [50°C]. This condition is specified by specimen designation S1. Following this treatment wear tests were performed on samples which were:

(1) double tempered, two 1 hours periods at 450°C (S2)

(2) glazed at 300 watts, then double tempered (SG1)

(3) glazed at 150 watts (SG2)

(4) glazed at 150 watts, then double tempered (SG3)

Electron beam surface area glazing was carried out using the technique previously described (1,3). Specimens were prepared with (i) a thick glazed layer ($\sim$100μm) using a beam power of 300 watts, and (ii) a thin glazed layer ($\lesssim$50μm) using a beam power of 150 watts. In addition to performing scanning electron microstructural observations and making precise weight-loss measurements the alloy phases within the wear debris were examined by x-ray diffraction.

The wear tests were carried out in a machine in which the end of a small cylindrical wear pin both impacted and slid across a steel counterface. Experiments were carried out using two counterface materials, the first of which was the moderately hard stainless martensitic steel, 17-4 PH. The other material was the molybdenum-base high speed steel M42 in which a 8wt% cobalt addition is used to produce hot hardness which is an important factor in wear. In all tests the transverse sliding velocity was 8 $m.s.^{-1}$ and the nominal maximum impact stress was 69M.Pa.

2.2. Wear against a Moderately Hard Steel.

In the first set of experiments both glazed and unglazed wear pins of SK material were tested against a 17-4 PH steel counterface. The hardness of this counterface material after heat treatment, prior to wear testing, was 400 DPN compared with a value of 950-1000 DPN for glazed and tempered SK, for example.

The general appearance of the near-surface layer of glazed SK following wear testing is typified microstructurally in Fig. 1(a). This cross-sectional view can, for convenience, be divided into four zones, the first of which (Zone A) is a layer of material transferred from the 17-4 PH counterface. Zone B, the glazed zone, is further separable into an upper heat-affected (tempered) deeply etched region 3-4μm below the near-surface and a lower more evenly etched dendritic carbide structure. Zone C is a region within the glazed zone where the tool steel has melted, yet has not reached a high enough temperature for complete dissolution of the original carbides. Zone D is representative of the morphology existing throughout the parent material. The overall morphological features just described are generally seen in all wear pins glazed to a depth of 50-100μm.

Figure 1(b) and (c) compare near-surface morphologies in two samples worn against 17-4 PH. Fig. 1(b) is a scanning electron micrograph of a glazed specimen with no post heat treatment. Note the thick adhered layer which, in view of the absence of detectable Ti levels (EDAX analysis), is almost completely 17-4 PH and the presence of nearly equi-spaced cracks which extend through the tranferred material and terminate near the base of the glazed zone. This is the same as was previously observed (1). Fig. 1(c) is a similarily glazed sample given a double tempered post treatment to increase martensite ductility and

thereby reduce the propensity for crack formation. A comparison of micrographs 1(b) and 1(c) reveals no significant differences. Evidence of cracking still exists, as does the layer of tranferred 17-4 PH counterface material. For the purpose of comparison the scanning electron micrograph in Fig. 1(d) shows the near-surface morphology in an unglazed sample of the SK material following wear testing under identical conditons. In this similar magnification micrograph it is clear that there is greater surface roughness. There is evidence of transferred material (Zone A) and, below this, a region plastically deformed in the sliding direction, with small fragmented carbides (Zone B). The actual amount of strain in the upper part of Zone B has been estimated from measurements of micrographs to be $\gtrsim$50%. Unlike the glazed wear specimens the cracks, in this case, occur only in the transferred material (Zone A). In an earlier study (1) precise measurements showed that both glazed and unglazed wear-pins either remained constant or slightly increased in weight following a test. In contrast, the counterface material (impact disc) underwent a heavy weight loss so that, in essence, there was "one body wear." Nevertheless, cross-sectional micrographs provide evidence that unglazed pins lose more material than do glazed pins. This is deduced, for example, from Fig 1(d) where carbide particles have clearly worked their way from the cemented carbide material into the adhered material (Zone A).

In Fig. 2 the weight loss is shown as a function of the number of impact cycles for both the glazed SK wear-pin and the 17-4 PH steel counterface; the sensitivity of the weight measurements is $\sim$0.1mg. Interestingly, no weight loss was observed for the pins, and, in fact, there was a detectable increase due to transferred counterface material. Also, a tempering treatment following electron-beam glazing apparently

had no effect. In marked contrast, the 17-4 PH counterface steel exhibited a significant weight loss both against tempered and untempered glazed wear-pins. The difference in the two curves for the counterface material in Fig. 2 may arise from relatively more material adhering to the tempered wear-pin.

In summary, the observations of glazed SK cemented carbide wearing against a 17-4 PH steel counterface show no evidence of massive material loss from the wear-pin or noticeable plastic deformation within the glazed near-surface material. However, there is the unattractive presence of cracks that extend throughout the adhered counterface layer into the glazed zone, this ultimately will lead to significant material loss.

2.3 Wear against a hard steel

When unglazed SK wear-pin specimens were tested against an M42 counterface the microstructure exhibited several features characteristic of wear against 17-4 PH. The cross-sectional micrograph in Fig. 3(a) from an untempered specimen shows there to be pronounced plastic deformation and carbide fragmentation limited in this case to the top 3-4μm. In contrast to wear against 17-4 PH however, examination of several randomly selected cross-sections did not reveal any evidence of the adhesion of counterface material. These tests on specimens of unglazed SK material showed that tempering had little effect on wear behavior. The only detectable difference, in fact, was a small amount of transferred M42 counterface material on the tempered SK wear-pins, see Fig. 3(b).

There are some interesting features in Fig. 4, which shows weight loss as a function of the number of impact cycles. Unlike wear against a moderately hard counterface steel (specifically 17-4 PH) Fig. 4 shows

that there is significant wear of the SK material as well as the M42 alloy counterface. Both tempered (S2) and untempered samples (S1) wear at a similar rate up to 50,000 cycles, beyond this there is a continued weight loss only for the untempered sample. A possible explanation for this is that a greater amount of counterface material adheres to tempered wear-pins (Fig. 3(b)) and that above 50,000 cycles the wear process is essentially M42 against M42, i.e. M42/M42 behaves as a highly resistant wear pair.

The wear of glazed SK material against M42 high speed steel has several distinctive features. These, as typified in Fig. 5 are a wear-pin with a particularly smooth surface and no detectable adhered counterface material. Furthermore, as seen in the deep glazed surface layer in Fig. 5, there is no cracking. There is some evidence of carbide fragmentation, but this is limited to the top 2-3μm of the glazed layer. A significant improvement in wear performance obtained by surface glazing is evident from the curve in Fig. 6, which is plot of weight loss vs. number of impact cycles. Comparison of this diagram with Fig. 4 shows that to obtain a weight loss equivalent to that of unglazed SK material it is necessary to increase the test-time by a factor of 2.5. (i.e. to 250,000 cycles). With this improvement in wear performance in a relatively deep glazed layer (~100μm) it is interesting to determine if wear characteristics are modified by reducing the as-glazed thickness. Specimens with a shallow glazed layer were wear tested and the microstructure in untempered and tempered specimens is seen in Figs. 7(a) and (b) respectively. In both cases wear has proceeded to the extent that the dendritic carbide zone (see Zone B in Fig. 1) has been removed. This, unfortunately, precludes any microsturctural assessment of the wear process. However, the weight loss curves (Fig.8) show the weight loss rate is comparable to that in the deep glazed zone

(Fig. 6) and it is considerably less than that of unglazed material (Fig. 4).

3. DISCUSSION

The present work shows that electron-beam surface area glazing is capable of improving the wear resistance of a hard cemented carbide material. Although the underlying mechanisms are imperfectly understood two important factors contributing to improved performance are the (i) high degree of homogeneity and (ii) high yield strength of the ultra-refined as-glazed microstructure. Before considering wear of glazed material it is first necessary to examine the degradation process in untreated material. The microstructure in Fig. 1(d) of unglazed material (against a 17-4 PH steel conterface) is indicative of a situation where fragmented carbide particles tend to align themselves along curved flow lines within a plastic deformation slip field produced by shear along the wear direction. X-ray diffraction analysis of wear debris shows that small TiC particles are carried from the SK material into the adhered layer.

Observations during actual wear tests indicate that an adhered layer of 17-4 PH forms at an early stage on the wear-pin surface. It is the continual breakaway and renewed build-up of this layer that produces the wear debris. The 17-4 PH readily shears from the counterface due to the plastic softening resulting from localized heating during sliding and impact. When, however, a sufficiently thick layer has been transferred to the wear-pin the adhered zone exhibits a hardness of about 800 DPN. The increase in hardness arises from a combination of precipitation hardening, mechanical mixing of alloy phases and oxides and the presence of untempered martensite formed as a result of wear test induced heat

treatments. In addition to being hard, microstructural observation of severe cracking shows Zone A structures to be rather brittle. Interestingly, the cracks in the adhered 17-4 PH layer do not propagate into the cemented carbide material. Presumably this is because the tool steel matrix readily accomodates the intensified stress field at the crack tip by plastic deformation. Although there are no detectable cracks within the near-surface region of the SK material a small amount of SK nevertheless, is removed. This, presumably, arises from the small amount of near surface material that is firmly bonded to the fragments of adhered 17-4 PH detaching itself during the wear process.

An important characteristic of the ultra-refined microstructure in glazed "Ferro-Tic" SK is its high resistance to plastic deformation. Although this is highly desirable in terms of improved microhardness it results in the continued propagation of cracks from the adhered layer into the actual wear-pin. This occurs because there is insufficient plastic deformation to relieve the intensified stress field at the crack tip.

From the experimental observations and the preceeding consideration it is evident that glazing is advantageous in improving wear resistance providing an appreciably thick, brittle and tenaciously adhered layer does not form. Such a conclusion is well supported by wear experiments using a hardened M42 steel counterface. In this case little or no detectable adhered layer is formed, presumably because the good hot hardness prevents plastic shearing. As well as an apparent absence of cracking in glazed "Ferro-Tic" SK material the weight-loss curves in Figs. 4 and 6 clearly show that glazing increases the wear-life by a factor of greater than 2.5. The material degradation, in this case, appears to be surface abrasion involving the continued removal of fine-

particles. The creation of such particles, naturally involves surface microcracking, but such cracks are highly localized since they do not penetrate the glazed surface layer. This type of wear process occurs in both the SK wear pin and the M42 counterface. In the glazed condition the fine particle fragmentation is reduced thus showing the benefical effect of electron beam surface area glazing in reducing wear.

4. SUMMARY

The main experimental observation made from this study and the important conclusions drawn are summarized for completeness in Table I below.

Table I

Ferro-TiC SK Wear Pin (Designation)	Counterface	Major Observations	Conclusions
Glazed	17-4 PH	17-4 PH adhered to "SK" wear pin. Equispaced cracks in "SK" glazed zone normal to sliding direction. Minimal surface texturing of "SK". Large weight loss from counterface. No detectable weight loss for wear pin.	Massive material loss of "SK" is reduced by electron beam surface glazing. Glazed zone cracking is is not reduced by tempering and and is related to the tenacity of the adhered layer and the inability of the finely interwoven dendritic structure of the glazed zone to accomodate plastic strain.
Glazed and Double Tempered	17-4 PH		
No Glaze	17-4 PH	Significant plastic deformation observed in pin cross-section, fragmented carbide carried into adhered layer very significant wear pin surface roughness.	

Ferro-TiC SK Wear Pin (Designation)	Counterface	Major Observations	Conclusions
No Glaze (S1)	M42	Very little M42 adhered to wear pin. Near surface plastic deformation and carbide fragmentation observed. Surface very rough. Weight loss data indicated material loss for wear pin and counterface.	Microstructural observations indicate that during the wear test material is disturbed only in the top 5μm of the near surface. M42/SK weight loss data is indicative of two body wear. The absence of weight loss for the S2 wear pin above 50,000 cycles probably arises from the adhered M42 layer which leads to a M42/M42 wear pair in the latter stages of the wear test.
No Glaze and Double Tempered (S2)	M42	Slightly more adhered material than above case (S1) Observations otherwise similar. Weight loss data comparable up to 50,000 cycles: above this pin wear is not detectable.	
Glazed and Double Tempered (SG1)	M42	No cracks in the glazed zone. Evidence of carbide fragmentation and loss is restricted to the top 2-3μm of the glazed zone. Wear pin weight loss is significantly reduced compared with S1 and S2 unglazed samples.	The absence of cracks in the glazed zone is related to the reduction in the adhered wear layer (M42). For this wear pair SK/M42, electron beam glazing increases wear life by ~2.5x.
Shallow Glaze (SG2)	M42	Glazed zone is completely removed down to the level of Zone C (Fig. 1(a)) during the wear test. Weight loss data consistent with that of SG1 wear pin.	The thin glazed zone resistance to wear is equal to the deep glaze SG1 up to the point of total zone removal.
Shallow Glaze and Double Tempered (SG3)	M42		

ACKNOWLEDGMENTS

The wear tests and debris analysis described in this report were performed by S. F. Wayne whose assistance, together with the advice of Professor S. L. Rice, is gratefully acknowledged.

REFERENCES

(1) B. G. Lewis, Annual Progress Report, Contract #N00014-78-C0580, July 1980, pgs. 40-43.

(2) B. G. Lewis, D. A. Gilbert and P. R. Strutt, Rapid Solidification, Principles and Technologies II, Ed. R. Mehrabian, B. H. Kear and M. Cohen, Claitors Publ. Div., March 1980, pg. 221.

(3) S. L. Rice, Wear 54, (1979), 291.

FIGURE CAPTIONS

(Figures 1, 3, 5 and 7 are SEM micrographs of wear pin sub-surfaces taken following mechanical polishing and etching in Vilella's reagent).

Fig. 1 (a) Electron-beam glazed SK Ferro-Tic wear pin sectioned parallel to the sliding direction; shown are the typical wear sub-surface zones present in glazed SK worn against a 17-4 PH counterface.
(b), (c) Glazed and glazed and tempered SK respectively worn against 17-4 PH. THe arrows indicate cracks in the glazed zone.
(d) Parent SK worn against 17-4 PH. Here cracks are only observed in the adhered Zone A.

Fig. 3 (a), (b) Austenitized and quenched SK(S1) and tempered SK(S2) worn against an M42 counterface.

Fig. 5 Glazed and tempered SK (SG1) worn against M42. Note the absence of cracks in the glazed zone following wear.

Fig. 7 (a), (b) Shallow glazed (SG2) and shallow glazed (SG3) and tempered Sk respectively worn against M42. The glazed zone has been removed during the wear test to the level of Zone C.

(Figures 2, 4, 6 and 8 depict the weight loss data for the above wear tests as a function of repetitive impact cycles. The weight loss is determined to an accuracy of 0.1 mg and data for both the wear pin and counterface are presented).

Fig. 2 Weight loss data for glazed SK Ferro-Tic worn against 17-4PH.

Fig. 4 Weight loss data for parent SK (S1 and S2) worn against M42.

Fig. 6 Weight loss data for (deep) glazed SK(SG1) worn against M42.

Fig. 8 Weight loss data for (shallow) glazed SK (SG2 and SG3) worn against M42.

AD-A107 559 CONNECTICUT UNIV STORRS INST OF MATERIALS SCIENCE F/6 20/5
ELECTRON BEAM/LASER GLAZING OF IRON-BASE MATERIALS.(U)
JUL 81 P R STRUTT, B G LEWIS, M KURUP N00014-78-C-0580
UNCLASSIFIED NL

2 OF 2
AD A
107 559

END
DATE FILMED
1-82
DTIC

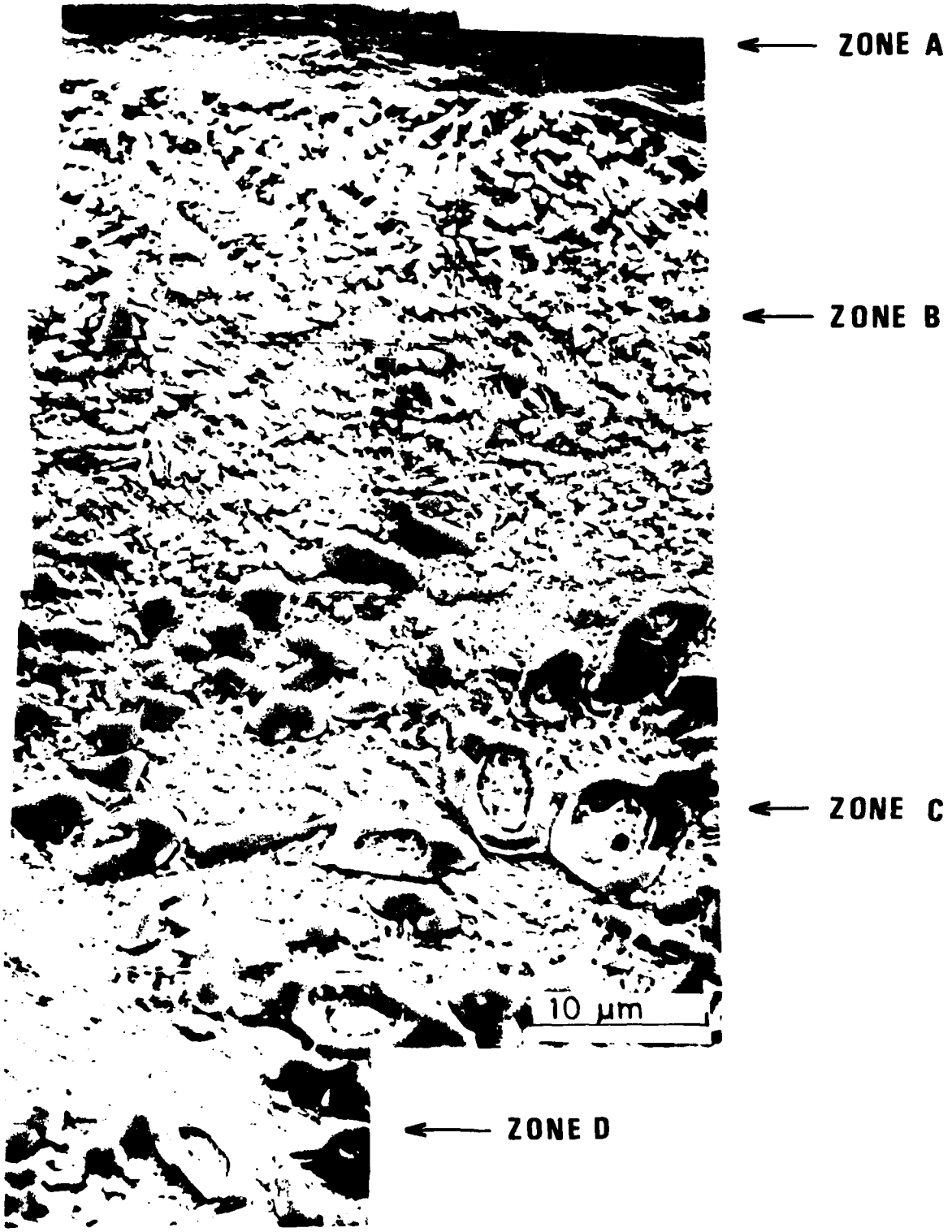

(a)

Fig.1

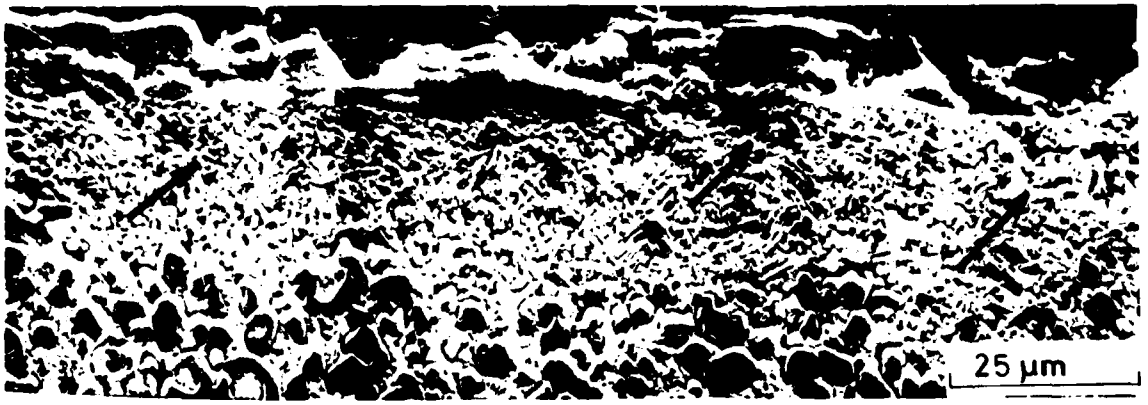

(b)

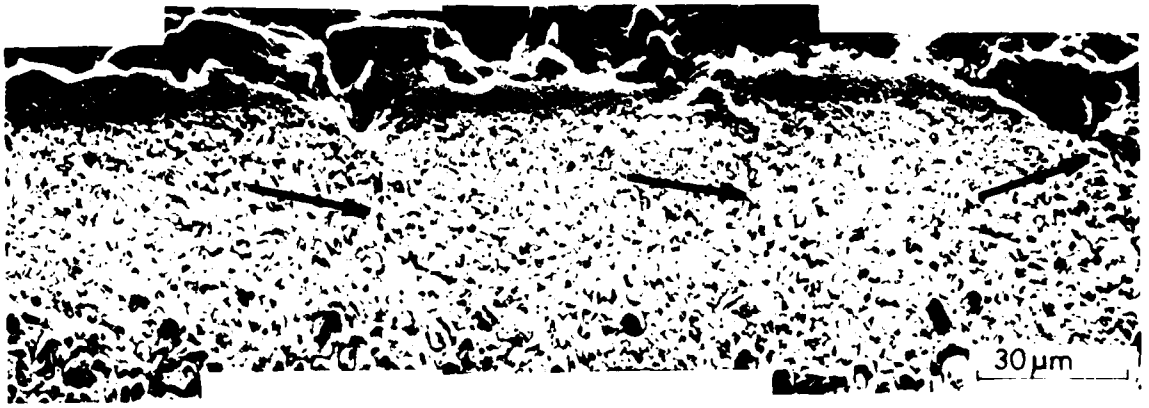

(c)

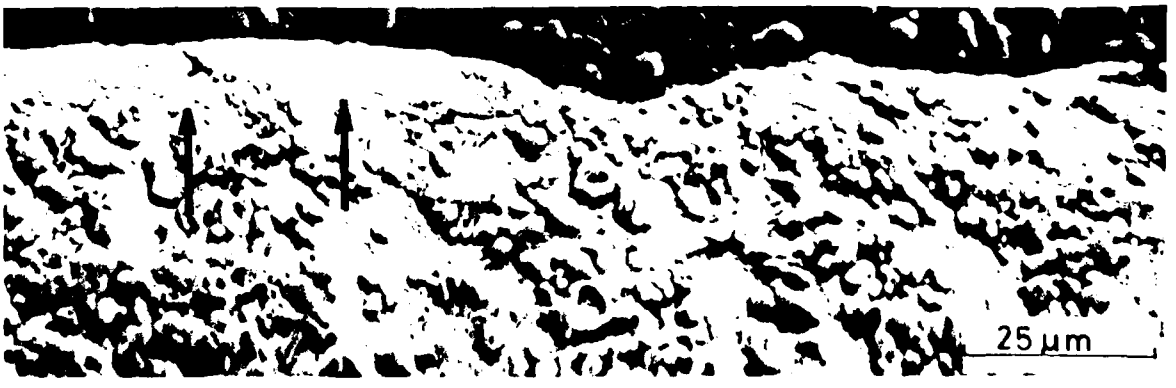

(d)

Fig .1 (contd.)

(a)

(b)

Fig.3

Fig.5

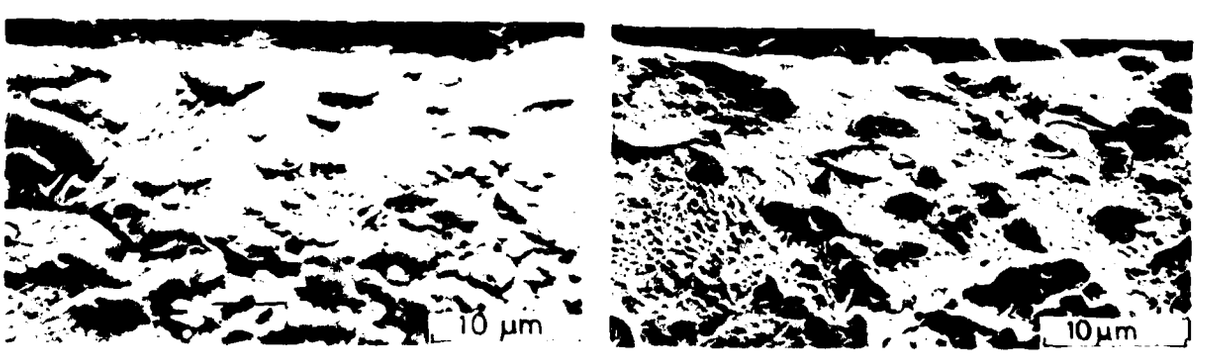

(a) (b)

Fig.7

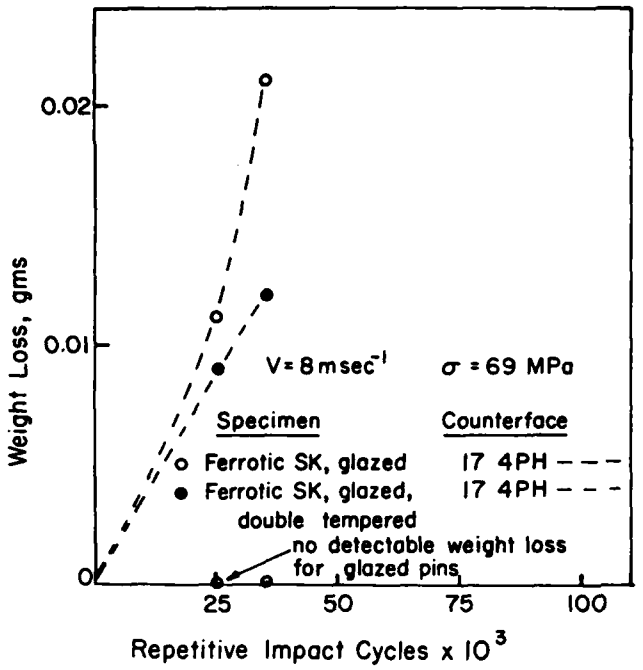

Fig. 2

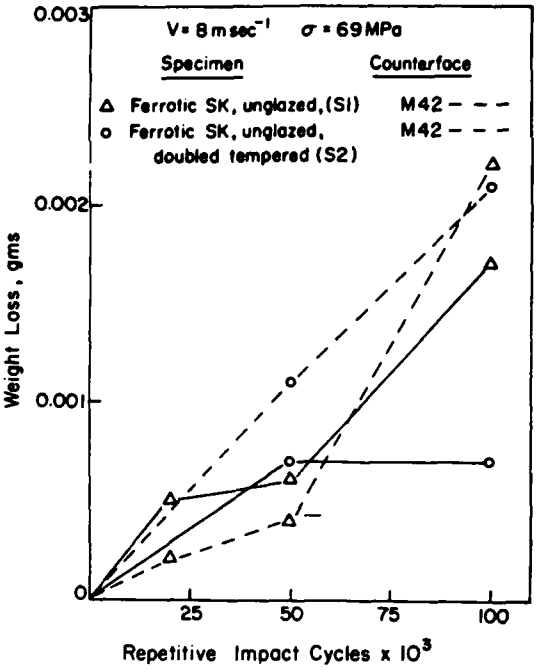

Fig. 4

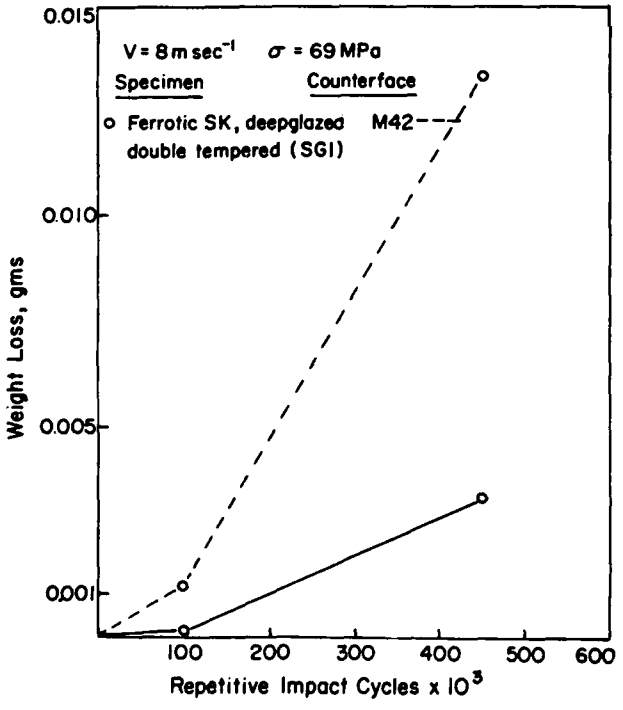

Fig. 6

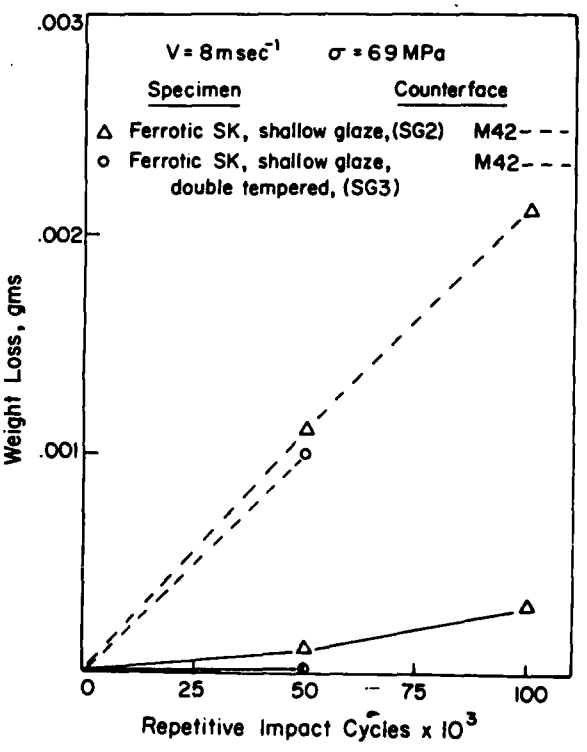

Fig. 8